J. Fluid Mech. (1998), *vol.* 372, *pp.* 323–355. Printed in the United Kingdom

© 1998 Cambridge University Press

Oscillations and breakup of a bubble immersed in a turbulent field

By FRÉDÉRIC RISSO AND JEAN FABRE

Institut de Mécanique des Fluides de Toulouse, UMR CNRS 5502,
Allée du Professeur Camille Soula, 31400 Toulouse, France

(Received 3 September 1997 and in revised form 31 March 1998)

This work is an experimental study of the deformation and breakup of a bubble in a turbulent flow. A special facility was designed to obtain intense turbulence without significant mean flow. The experiments were performed under microgravity conditions to ensure that turbulence was the only cause of bubble deformation. A scalar parameter, characteristic of this deformation, was obtained by video processing of high-speed movies. The time evolution and spectral representation of this scalar parameter showed the dynamical characteristics of bubble deformation. The signatures of the eigenmodes of oscillation predicted by the linear theory were clearly observed and the predominance of the second mode was proved. In addition, numerical simulations were performed by computing the response of a damped oscillator to the measured turbulence forcing. Simulations and experiments were found to be in good agreement both qualitatively, from visual inspections of the signals, and quantitatively, from a statistical analysis. The role of bubble dynamics in the deformation process has been clarified. On the one hand, the time response of the bubble controls the maximum amount of energy which can be extracted from each turbulent eddy. On the other hand, the viscous damping limits the energy that the bubble can accumulate during its fluctuating deformation. Moreover, two breakup mechanisms have been identified. One mechanism results from the balance between two opposing dominant forces, and the other from a resonance oscillation. A new parameter, the mean efficiency coefficient, has been introduced to take into account the various aspects of bubble dynamics. Used together with the Weber number, this parameter allows the prediction of the occurrence of these two mechanisms. Finally, the influence of the residence time of the bubble on the statistics of the deformation has been analysed and quantified.

1. Introduction

One of the major issues in the study of bubbly flows is the prediction of the bubble size. This problem has motivated several investigations on the breakup of bubbles or droplets. In the thirties, Taylor (1932, 1934) led the way by studying the deformation of droplets caused by viscous stress. Two decades later, Hinze (1955) summarized the state of the art in a famous paper in which he proposed the first classification of the causes of deformations (viscous stress, dynamic pressures) for different kinds of flows (laminar parallel, Couette, rotating, turbulent, etc.). He attempted to relate these causes within a universal framework based on a simple force balance. Flow around the bubble produces a stress T that causes deformation. This is counteracted by the surface tension σ that tends to restore the bubble shape by inducing a stress of the order σ/d, where d is the bubble diameter. The ratio of these two stresses gives the dimensionless group N which characterizes the deformation, $N = Td/\sigma$. When the viscous forces

control the flow, N is a capillary number ($T = \mu S$, with S the shear rate and μ the viscosity) whereas when inertia dominates, it is a Weber number ($T = \rho U^2$, with U the continuous-phase velocity and ρ the density). But in all cases the breakup is expected to occur when the value of the dimensionless group N exceeds a critical value.

Although this approach has been fruitful, its limits are obvious today. The use of a critical value as a breakup limit is probably only valid for the case of an initially spherical droplet or bubble placed in a steady flow (see Stone & Leal 1989). Furthermore, the corresponding critical value depends on the kind of flow and on the physical properties of the two fluids, i.e. their viscosity and density. A remarkable diversity of breakup mechanisms has been observed. As a consequence each study has focused on a specific case. In the present study, we are interested in the breakup mechanism occurring in turbulent flows.

Because of the random character of the turbulent fluctuations, the turbulent situation is extremely complicated. First the flow is not steady. Secondly, the spatial structure of the velocity field in the vicinity of the bubble is unknown and depends on the characteristics of the different eddies that are present at a given instant. Several investigators (Zeitlin & Tavlarides 1972; Coulaloglou & Tavlarides 1977; Calabrese, Chang & Dang 1986*a*; Calabrese, Wang & Bryner 1986*b*; Wang & Calabrese 1986) used very complex turbulent flows, such as those obtained in stirred tank, to study the diameters of a population of inclusions. These experiments, though technically interesting, do not improve our understanding of the breakup mechanism. Fundamental studies of isolated bubbles or drops in a simple geometry were generally limited to turbulent pipe flows. Most of these studies deal with drops of organic liquid put in tap water (Sleicher 1962; Swartz & Kessler 1970; Collins & Knudsen 1970; Karabelas 1978). However, some authors used air bubbles in water (Walter & Blanch 1986; Hesketh, Etchells & Fraser Russell 1987, 1991). Apart from pipe flows, only two other experimental studies are known. Sevik & Park (1973) injected bubbles in the axis of an upward turbulent jet. Senhaji (1993) used a downward uniform turbulent flow in which the turbulence was generated by the passage of the flow through a grid, and the downward mean flow was adjusted in order to keep the bubble still on average.

Surprisingly, in spite of the complexity of the problem, all these investigations were essentially confined to the experimental determination of the maximum stable diameter. They have in common the use of the only available theory for breakup in turbulent flows, independently proposed by Kolmogorov (1949) and Hinze (1955). This theory is based on two fundamental assumptions: (i) for eddies larger than the Kolmogorov microscale, inertia dominates, (ii) only velocity fluctuations over a distance close to the bubble diameter are capable of causing large deformations. Therefore the stress T responsible for the bubble deformation can be written $T = \rho\,\overline{\delta u^2(d)}$ where ρ is the density of the continuous phase and $\overline{\delta u^2(d)}$ is the mean-square velocity difference over a distance equal to the bubble diameter. This gives the following expression for the Weber number: $We = \rho\,\overline{\delta u^2(d)}\,d/\sigma$. The theory then postulates the existence of a critical value beyond which breakup occurs.

Limiting the analysis to such an approach is necessarily very restrictive. Delichatsios (1975) was the first to suggest that the above expression for the Weber number is not correct even if the force balance model is acceptable. Rigorously, the maximum value $\max(\delta u^2(d))$ instead of its average should be used. This author introduced the breakup rate per unit time by using the probability for the instantaneous turbulent intensity to exceed a given threshold. But this notion is not useful in practice because our present knowledge of the turbulence statistics does not allow us to calculate the corresponding probabilities. Nevertheless, this argument raises an important question for the

experiments. For determining the maximum stable diameter of the inclusion in a given turbulent field, the residence time of the bubble in this field has to be large enough to ensure that the bubble has experienced the largest possible turbulent fluctuation. But the definition of 'large enough' is not straightforward, and has been the subject of debates between various authors and it can explain a number of discrepancies observed in the results of various studies performed in turbulent pipe flows. Up till now, the residence time of the bubble in the turbulent field was never taken into account. All the authors postulated that the residence time was large enough without carefully checking this assumption.

A second argument is that there is no evidence to support the claim that breakup depends solely on a critical value of the Weber number, although this number is undoubtedly a relevant parameter. The interpretation of breakup in terms of a force balance is not unique. In fact, it completely ignores the dynamics of the bubble response to unsteady perturbations. Recently, Shreekumar, Kumar & Gandhi (1996) performed numerical simulations of the response of a drop to a single external pressure fluctuation. The results were extended to real turbulent situations by using the classical scaling of turbulent eddies and assuming that no coherent interaction between successive eddies exists. Thereby, they extended the force balance approach to take into account the dynamical response of a drop to a single eddy, but they ignored the role of eddy succession. In contrast, Kang & Leal (1990) used a model equation to study the dynamics of the bubble shape in periodic straining flows. They found that when the excitation frequency was close to the natural frequency of the bubble, large deformations are promoted. In such a case, it is clear that the amplitude of deformation depends not only on the instantaneous turbulence intensity but also on the occurrence frequency of the turbulent eddies. To our knowledge, only Sevik & Park (1973) analysed turbulent breakup by postulating a resonance mechanism between the bubble dynamics and the turbulent fluctuations. They suggested a matching of a characteristic turbulence frequency with the lower natural frequency of bubble oscillation. Unfortunately, their approach led to exactly the same result as the theory of Kolmogorov–Hinze, since they also demonstrated the existence of a critical value of the Weber number beyond which the breakup occurs. It is thus impossible to determine which is the correct interpretation.

Finally, another problem limits the interpretations of breakup experiments in turbulent flows. Generally, the viscous force induced by the mean velocity gradient and the mean bubble drift caused by buoyancy mix their effect with that of turbulence to control the bubble shape. In pipe flows, breakup was most often observed close the wall where the intense gradient of the mean velocity participates in the deformation. The experiment of Senhaji (1993) used a uniform turbulent downward flow in order to eliminate the mean velocity gradient, but the mean drift induced by buoyancy was another important cause of deformation. Thus, in the aforementioned situations, the random action of the turbulence was always superimposed on a previous deterministic deformation.

In the present study the specific effect of turbulence upon the bubble deformation and breakup is analysed. An experimental investigations of bubble deformation in a turbulent field with neither significant mean motion nor buoyancy was realized with the aim of answering three questions: What is the amount of turbulent energy necessary to cause breakup when the turbulence is the only cause of deformation? How do bubble dynamics and turbulence interact to control deformation? How does the deformation statistics depend on the residence time of the bubbles in turbulence?

2. Experimental facility

To study the specific effect of the turbulence on bubble deformation, an original experimental device was designed. It satisfies the two following constraints: (i) obtaining a test section in which an intense turbulence is maintained in the absence of a significant mean motion, (ii) eliminating the mean bubble drift induced by buoyancy. The ideal flow field would be: zero mean velocity and stationary, homogeneous and isotropic turbulence. Isotropy would permit ignoring the orientation of the bubble deformation. Homogeneity would allow the bubble location to be unimportant. Moreover, stationarity is required for studying the bubble response to turbulent time scales and not to arbitrary variations of the boundary conditions. However, to obtain a turbulent zone where the fluctuations are large compared to the mean velocity is a difficult challenge. Nevertheless, a good approximation of this ideal flow has been attained by using a turbulent axisymmetric jet discharged into a closed tube. This flow, exhaustively described in a previous paper (Risso & Fabre 1997), corresponds to situations in which the turbulence is dominated by turbulent transport. For the sake of clarity, only the results relevant for the analysis of bubble breakup will be recalled. In addition to this, the experiments were carried out at microgravity conditions to cancel buoyancy. The experimental set-up was specifically designed to be used aboard the Caravelle Zero-G of the Centre National d'Etudes Spatiales, this special aircraft being able to produce microgravity conditions during parabolic trajectories.

A schematic diagram of the experimental device is shown in figure 1. The system consists of three parts, the water loop, the bubble supplier and the video equipment. The water loop is designed to produce the turbulent field in a cylindrical glass tube of diameter $D = 77$ mm and 600 mm length. The tube is closed at one end. Both liquid inlet and outlet are located at the other end. The fluid enters through a circular central nozzle of 15 mm diameter and flows out through an annular passage of 70 mm inner diameter and of outer diameter equal to the tube diameter D. Water is supplied to the nozzle by a centrifugal pump of 1700 W from a 100 l constant pressure tank. At the tube outlet, the water flows through a calming zone back to the tank.

The kinematic structure of the flow field in the test section has been measured in the laboratory by using laser doppler anemometry. Hereafter, U denotes the mean velocity, u the fluctuating velocity, z the distance from the inlet, and the overbar represents time average. It was established that the turbulence is everywhere fully developed, statistically stationary, stable and reproducible. The velocity spectrum is continuous without any privileged frequency and exhibits an inertial subrange with the classical $-5/3$ power law. Far from the inlet, the confinement causes a rapid decrease in the mean jet velocity, whereas the decrease in the turbulence intensity is slower. At a distance of about $3D$ ($z = 230$ mm), the role of the mean flow becomes negligible. From this location, the kinetic energy of the mean flow remains less than that of the turbulence by one order of magnitude. The flow is mainly controlled by a turbulent transport–dissipation balance. At a distance of $4.4D$ ($z = 340$ mm) an asymptotic state of the turbulence behaviour is achieved. Its properties may be summarized as follows:

(i) The flow is self-preserving in the axial direction z.

(ii) All the statistical moments of the velocity decrease with z according to the same exponential law. In particular, the standard deviation decays exponentially with distance as

$$\overline{u^2}^{1/2} = (\overline{u_r^2} + \overline{u_\theta^2} + \overline{u_z^2})^{1/2} = \overline{u^2(z_0)}^{1/2}\, \mathrm{e}^{-(z-z_0)/D}. \tag{1}$$

(iii) The largest turbulent scales are locked to the tube diameter. As a consequence,

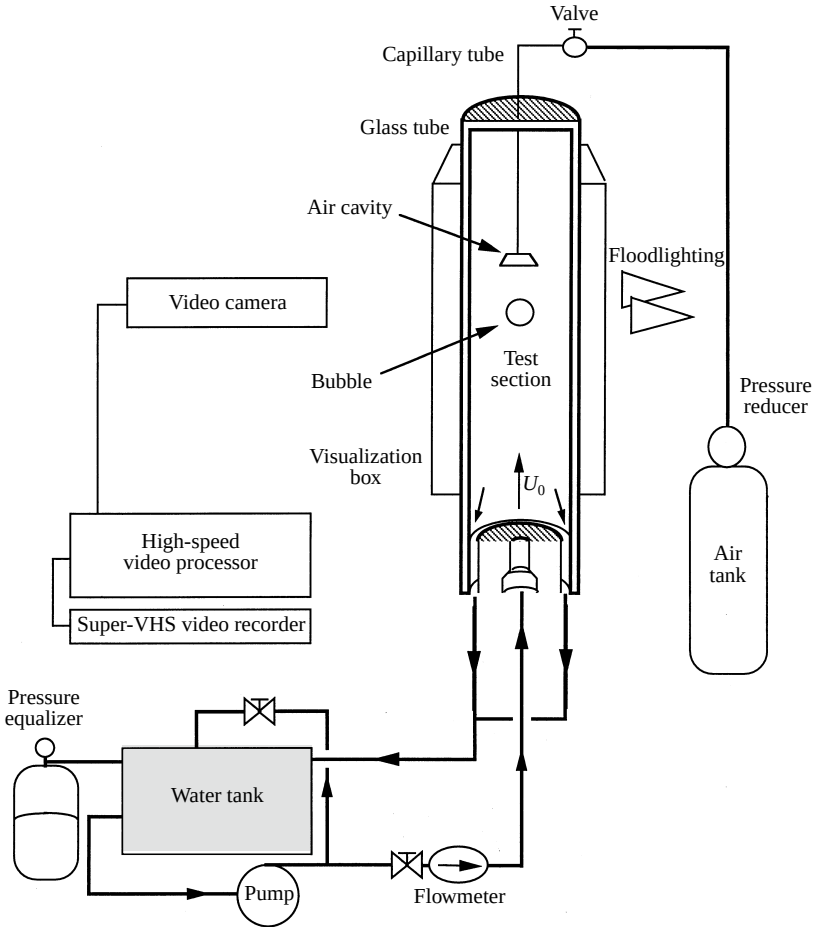

FIGURE 1. Experimental apparatus.

the integral turbulent length scales remain constant (the value of longitudinal integral scale Λ being $0.27D$).

(iv) In the central part of the tube, the Reynolds tensor is isotropic and homogeneous in each cross-section.

Therefore, except for the inhomogeneity in the axial direction, this turbulent zone has the desired properties.

A turbulent intensity large enough to cause the breakup of an air bubble of the order of a centimetre is also required. The flow structure being independent of the inlet Reynolds number, the turbulent intensity could in principle be adjusted by simply varying the inlet velocity. As shown below, the required level of turbulence is very large. The most powerful pump compatible with the plane requirements led to an ejection velocity fixed at $U_0 = 10$ m s^{-1}. This velocity corresponds to an inlet Reynolds number based on the nozzle diameter of 150000. With these flow conditions, the turbulent test section for studying bubble breakup had to be located in a region where the turbulence has not reached its asymptotic behaviour ($300 < z < 400$ mm, $3.9 < z/D < 5.2$). Nevertheless, the flow properties in this test section are the same as in the asymptotic region except that complete isotropy of the Reynolds tensor is not attained

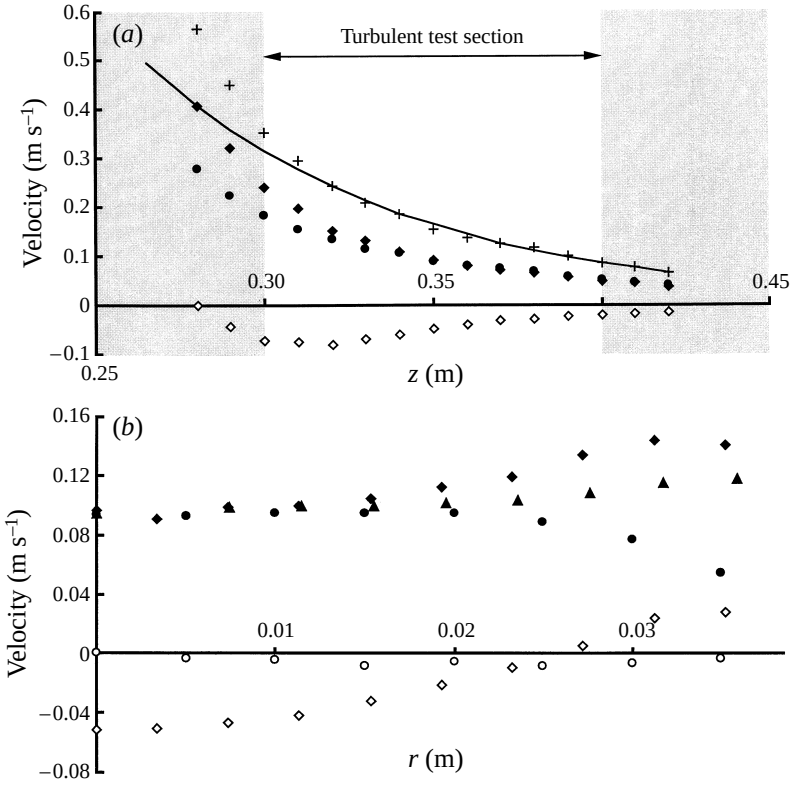

FIGURE 2. Mean and r.m.s. velocities in the test section: (*a*) at the axis and (*b*) radial evolution at $z = 0.35$ m. ◇, U_z; ○, U_r; ◆, $\overline{u_z^2}^{1/2}$; ●, $\overline{u_r^2}^{1/2}$; ▲, $\overline{u_\theta^2}^{1/2}$; +, $(\overline{u_z^2}+\overline{u_r^2}+\overline{u_\theta^2})^{1/2}$; ——, equation (1).

for $z < 340$ mm. At worst the ratio of the standard deviation of the axial to the radial velocity is equal to 1.3. Figures 2(*a*) and 2(*b*) show the axial and radial profiles of both average (open symbols) and standard deviation (filled symbols) of the velocity components (axial: diamonds, radial: circles, azimuthal: triangles). It can be seen that the mean flow is negligible and that the turbulence homogeneity and isotropy are more than satisfactory. In addition, the turbulent level $\overline{u^2}^{1/2}$ (crosses on figures 2*a*) decays from 35 to 8.5 cm s^{-1} in the test section.

The results presented in this paper were obtained during two campaigns of parabolic flights. Each campaign consisted of three flights of thirty parabolas. The relative gravity in each direction was measured by accelerometers fixed on the experimental set-up. Each parabola was composed of three successive stages of 20 s: the acceleration stage in super-gravity (~ 18 m s^{-2}); the microgravity stage during which the residual gravity fluctuations had a main frequency close to 0.3 Hz and amplitude less than 0.4 m s^{-2}; the decelerating phase with again 18 m s^{-2}. Each parabola was preceded by 2 minutes of horizontal flight. Air was injected during the normal gravity period by opening a valve (see figure 1). It was stored in an 10 MPa tank and flowed through a pressure reducer before entering, at 0.2 MPa, in a capillary tube to fill up a cavity located near the top ($z = 500$ mm). The air volume so formed could be varied from 4×10^{-3} to 5 cm^3. It was maintained by gravity in the cavity which was only opened at its bottom. The capillary tube was used to avoid turbulent pressure fluctuations that cause volume variations in the air supply system. A pressure equalizer maintained the pressure at the fixed value of 0.15 MPa, independent of the volume of air introduced

in the loop. After the acceleration stage, the microgravity allowed the volume of air to form a spherical bubble that became free to move within the test section.

A visualizing box permitted the observation of the bubble without optical distortion. The test was recorded with a high-speed digital video camera Kodak Ektapro EM at a rate of 500 frames s^{-1}. Only the period during which the bubble was inside the test section ($300 < z < 400$ mm) was used for the analysis. After each parabola, normal gravity was restored and the air was evacuated by a valve located at the top of the tube. The video sequence was recorded onto an analogue standard S-VHS tape and the digital memory of the camera was cleared. The experimental device was then ready for the next parabola.

3. Extraction of bubble characteristics by video processing

All the information that characterizes the bubble shape has been extracted from the images. The calibration was performed by filming objects of known size placed inside the test section. By this method, the scale factor of the whole optical system (water, glass tube, optical box, lens) was accurately determined. We found that the calibration depended on the distance between the bubble and the camera (y-direction). As the location of the bubble in this direction was unknown, the calibration corresponding to the tube axis was always used. The resulting error increases linearly with the y-coordinate and ranges between -7% to $+7\%$.

The bubble evolution was analysed by video processing, with in-house software (Bongiovanni 1996; Bongiovanni, Chevaillier & Fabre 1997). The black and white pictures were digitized into a 256×256 pixels matrix using 256 grey levels. Only one picture out of four was used, giving 125 frames s^{-1} digitized movies. After detection of the bubble and binarization of the pictures, the projection of the bubble on the plane of visualization (xOz) was described by a connected set of pixels. Several geometrical parameters were determined from this set. The bubble location was characterized by its centre of gravity and by its limits in both the axis (z-direction) and the transverse (x-direction) directions. The location of these limits was used to stop the analysis as soon as the bubble reached the test section limits. For the analysis of the deformation, four parameters were tested: the perimeter, the area, the inertial moments and an estimation of the maximum chord of the contour. Although the maximum chord is the most natural parameter characterizing the deformation, it was difficult to find an effective algorithm for its determination in cases of very complex shapes. There are three other basic parameters for the description of the two-dimensional object. Their evolution with time exhibited quite similar behaviour (Risso 1994). For the perimeter, only the boundary pixels were taken into account, whereas all the pixels were used for the area. Each pixel was a square of 0.5 mm side. The smallest bubble under investigation had a diameter of 12.4 mm, i.e. 67 pixels for the perimeter, 354 for the area. The largest bubble had a diameter of 21.4 mm, i.e. 138 pixels for the perimeter, 1514 for the area. Because of the small errors made in the determination of the bubble boundary, the perimeter evolution is very noisy in contrast to the area evolution which is smooth. The inertial moments present intermediate behaviour since all pixels are used but those close to the boundary have a greater contribution. Moreover, they also required the estimation of the centre of gravity. Consequently, for accurate and reproducible results, only the results based on the bubble projected area A will be presented here. In fact, the resolution was large enough to ensure that bubble detection and binarization errors on the area were negligible compared to those related to calibration.

In what follows, we shall use the relative difference of the projected area with respect to that of the sphere, defined by

$$A^* = \frac{4A}{\pi d^2} - 1 \tag{2}$$

since it is more representative of the deformation (d is the diameter of the non-deformed bubble). Unfortunately, this parameter was determined from two-dimensional pictures. Thus, the consequences of the projection have to be determined. In relation to this, the projection of the shape when the bubble is submitted to linear oscillations was calculated.

Each eigenmode of the linear solution of the bubble vibration (Rayleigh 1879; Lamb 1932) is characterized by two integers n and m such that $n \geqslant 2$ and $0 \leqslant m \leqslant n$. In spherical coordinates, the local radius of the deformed bubble is given by

$$\left.\begin{aligned} r &= \tfrac{1}{2}d(1+\epsilon_{nm}\cos(m\phi)\,P_{nm}(\cos\theta)\cos(2\pi f_n t)), \\ P_{nm}(x) &= (-1)^m(1-x^2)^{m/2}\frac{\mathrm{d}^m P_n(x)}{\mathrm{d}x^m}, \end{aligned}\right\} \tag{3}$$

with

$$f_n = \frac{1}{2\pi}\left(8(n-1)(n+1)(n+2)\frac{\sigma}{\rho d^3}\right)^{1/2}, \tag{4}$$

where θ and ϕ are the azimuthal and the meridian angles, t is the time, ε_{nm} is the amplitude of mode (n, m), and P_n are Legendre polynomials. The linear theory applies for $\varepsilon_{nm} \quad 1$ and the evolution of the bubble shape is given by a combination of these modes. The most general expression is then

$$r = \tfrac{1}{2}d(1+\sum_n\sum_m \varepsilon_{nm}\cos(m(\phi-\phi_{0nm}))\,P_{nm}(\cos\theta)\cos(2\pi f_n(t-t_{0nm}))), \tag{5}$$

where the initial conditions fix the amplitudes ε_{nm} and the phases ϕ_{0nm}, t_{0nm} of each mode. The software developed for the present study permitted the computation of the local bubble radius (equation (5)) for any combination of modes. Then, for each computed shape, the bubble projected area A^*_{xy} (resp. A^*_{xz}) on the plane xOy (resp. xOz) was calculated numerically (Oz being the axis of symmetry of modes $m = 0$). Three different signatures of the bubble deformation were determined from the simulations: the local radius at $(\theta, \phi) = (0, 0)$ as the reference signature: it is a sum of cosines of frequency f_n and, as for area, we will use its relative variation $r^*(t) = (2r/d-1)$; the projected areas $A^*_{xy}(t)$ and $A^*_{xz}(t)$ to be analysed.

The computations were performed for all the values of n up to 7 and for all the values of m up to 5. In each case the maximum amplitudes were set to 20 % ($\varepsilon_{nm} = 0.2$) and the phases to zero ($\phi_{0nm} = 0$, $t_{0nm} = 0$).

Figures 3(*a*) and 3(*b*) present the results corresponding to the sum of the axisymmetric modes corresponding to $n = 2$, 3, 4 and $m = 0$. The time evolution of the local radius (thickest line on figure 3*a*) is not periodic because the frequencies of the different modes are not commensurate. The evolution of the projected areas (the two thinnest lines on figure 3*a*) differs from that of the radius. Their amplitude is smaller and depends on the plane of projection. Figure 3(*b*) features the power spectral densities of the projected area. The spectrum of the local radius is not shown here. It consists of three Dirac delta functions centred in f_2, f_3 and f_4. The projected area spectra are more complex, with six peaks centred at the following frequencies: f_2, f_4-f_2, $2f_2$, f_4, $2f_3$, f_4+f_2. If the presence of modes $n = 2$ and $n = 4$ is detected through the peaks at f_2 and f_4, the presence of mode $n = 3$ is only shown by a peak at $2f_3$. Furthermore, the energy

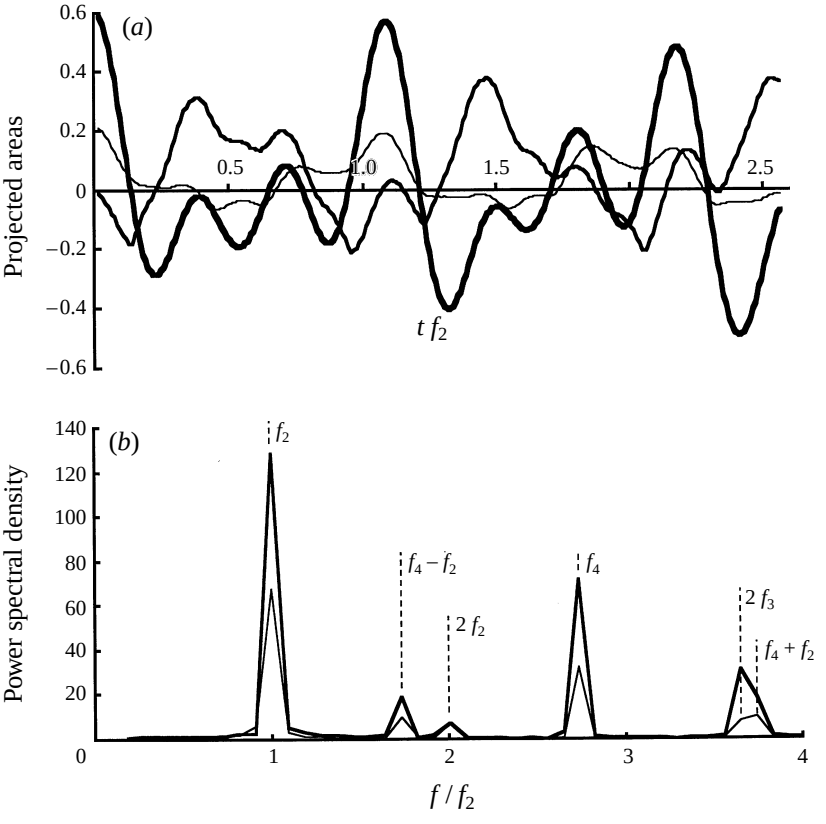

FIGURE 3. Projected area for the sum of the three first modes ($n = 2$, 3 and 4): (*a*) time evolution, (*b*) spectral evolution: ▬, r^*; ▬, A^*_{XY}; ——, A^*_{XZ}.

of the peak corresponding to mode $n = 2$ (f_2) is larger than that of mode $n = 4$ (f_4), itself larger than that of mode $n = 3$ ($2f_3$). Finally, the peaks corresponding to the interactions between modes are visible.

The analysis of numerical simulations involving various combinations between modes allows us to draw the following general conclusions about the measurable quantities. The nonlinearity of the projection operator greatly complicates the interpretation of the dynamics of the measured signature. In the spectral domain, even for an isolated eigenmode, a monochromatic signal is not obtained: higher-order harmonics are present. Moreover, the peak of lowest frequency depends on the parity of n. For even n, the natural frequency f_n and its harmonics (kf_n) are observed; for odd n, twice the natural frequency ($2f_n$) and its harmonics ($2kf_n$) are observed. When a sum of modes is considered, the projection operator causes an artificial interaction between modes. The peaks corresponding to addition or subtraction of the natural frequencies are visible. Therefore, it cannot be concluded that the presence of such peaks in the measured signals corresponds to a nonlinear effect of the bubble dynamics. The energy of each peak is related in a complex manner to the amplitude of the corresponding mode. It depends on n, m and on the plane of projection. Thus, the intensity of each peak cannot be easily interpreted. However, there exists a general tendency. The higher the order of a mode (large n), the weaker the intensity of the corresponding peak. The projection operator acts as a low-pass filter. In fact, when the bubble shape is complex, there are hidden parts, invisible on the projection, so that the energy measured at the

Class	Number	d_{min} (mm)	d_{max} (mm)	d_{avg} (mm)	Number of breakups	$f_{2\,min}$ (Hz)	$f_{2\,max}$ (Hz)	τ_{min} (s)	τ_{max} (s)
A	59	2	6	4.1	0–0 %	28	146	0.050	0.45
B	56	12.4	21.4	18	27–48 %	4.2	9.4	1.9	5.7

TABLE 1. Characteristics of the bubbles

corresponding frequency is less than expected. Besides, as a high-order mode induces stronger curvatures and requires, for a same amplitude ϵ_{nm}, a greater amount of energy than a lower order mode, we do not expect to find the signature of high-order modes in the experimental signals.

A similar study using the perimeter of the projected bubble instead of its area would lead to the same conclusions. The limitations introduced by the projection cannot be avoided by the choice of another geometrical parameter.

4. Qualitative description of the breakup process

Tap water was used as the continuous phase and air for the bubbles. The surface tension was $\sigma = 0.07$ N m$^{-1} \pm 5\,\%$. During microgravity, one bubble at a time was put into the region of negligible turbulence ($z \sim 450$–500 mm), out of the test section. Most often, we observed that the bubble moved slowly from the weak to the high turbulence region. The bubble behaviour was studied from the moment it entered the test section at the upper z limit ($z = 400$ mm) up to the moment it went out, generally at the lower z limit ($z = 300$ mm). Two populations of bubbles were studied, hereafter referred to as class A and B (see table 1): In class A, the bubble diameters ranged from 2 to 6 mm and the residence times from 1 to 3 s. No breakup was observed and, in every case the shape variations remained moderate. In class B, the bubble diameters ranged from 12 to 21 mm and the residence times from 0.25 to 2.5 s. Large deformations were observed, leading to breakup in about 50 % of cases. Thus, the present results on deformation and breakup concern bubbles of class B. Before discussing these results, it must be pointed out that the period of residual gravity fluctuations (~ 3 s) was greater than the bubble residence time (< 2.5 s), and much greater than the largest natural bubble period (0.24 s). Therefore, only the turbulent time scales were able to excite the bubble.

Figure 4 shows some typical sequences of bubble deformation. The observation of bubble deformation reveals the extraordinary diversity of shapes of the bubbles. Among them, the three types of shape (lenticular, cigar-shaped and bulgy) defined by Hinze (1955) can be identified. Although the statistical properties of the turbulence were the same for all the runs, the few seconds of turbulence experienced by each bubble were different. Consequently, each deformation history was unique. Sometimes, after a complex succession of shapes, the bubble left the test section without breaking up (runs 1 and 2). While at other times, breakup occurred (runs 3–6). The breakup events fall roughly into two categories. Breakup of the first category was the most likely ($\sim 80\,\%$ of runs). It occurred when the bubble reached its maximum lengthening (runs 3 and 5). In the simplest case, the bubble first took a cigar shape (type 2 of Hinze), then a dumbbell shape and finally split into two parts. In other cases, the shape was more complex and more than two fragments, namely three to ten, were produced. The diameter of each fragment was of the same order of magnitude as the initial bubble. In the second breakup category (runs 4 and 6), the splitting occurring after the bubble

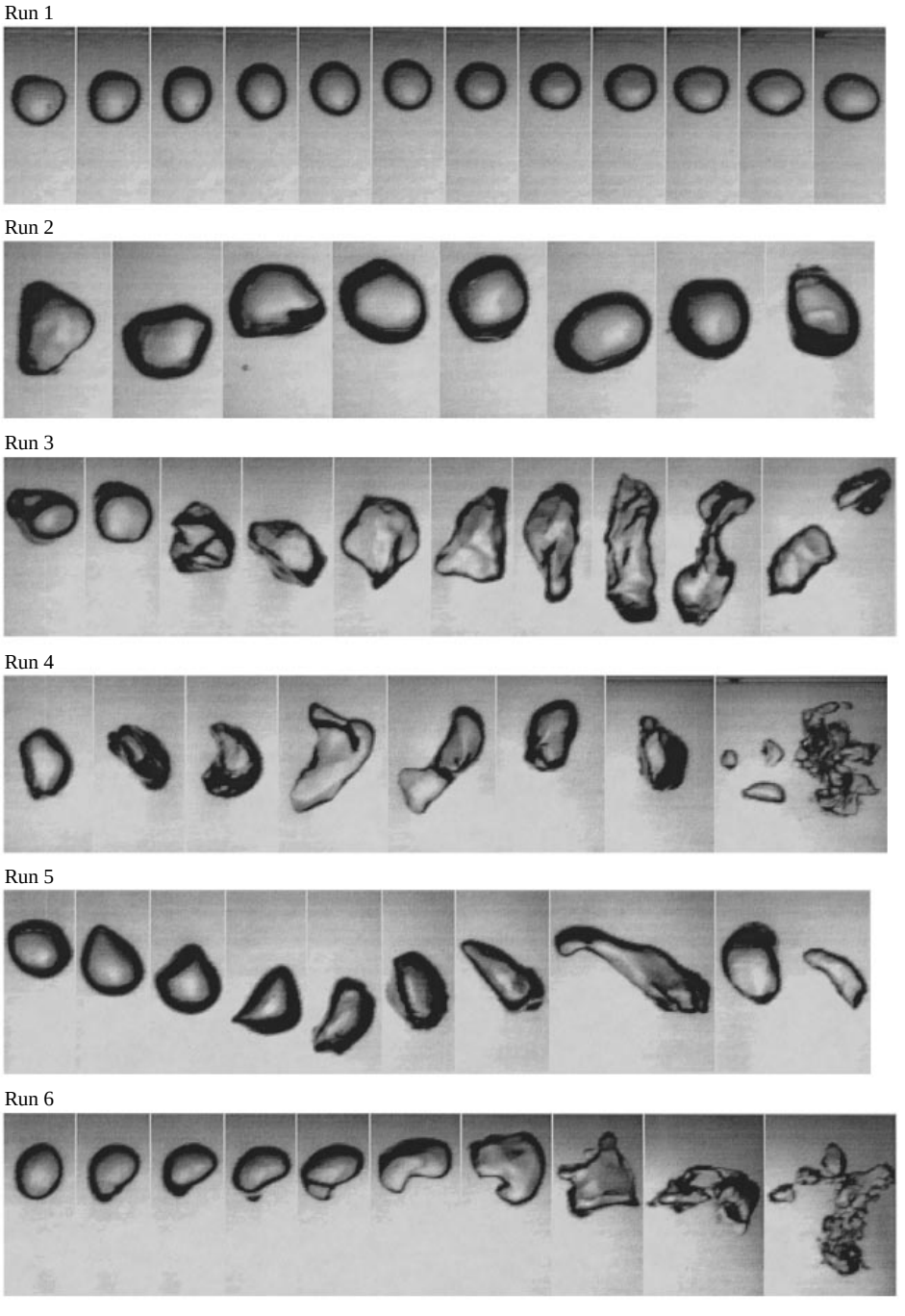

FIGURE 4. Sequences of experimental bubble deformations.

was flattened. The bubble experienced first a lenticular shape (type 1 of Hinze), then a bulgy shape (type 3 of Hinze) and finally the splitting produced numerous small fragments which were too small for their diameter to be determined.

Despite the diversity of events, some general conclusions can be drawn. The probability of breakup was strongly correlated with the maximum deformation

experienced by the bubble. This was clearly demonstrated by the experimental relation found between the maximum projected area A^*_{max} and the corresponding percentage of breakup: no breakup for A^*_{max} less than 0.5, 75% of breakup for A^*_{max} between 0.5 and 1, and 100% of breakup for A^*_{max} greater than 1. Furthermore, the bubble was always significantly lengthened before it broke, even in situations in which breakup finally occurred in the flattening stage of the deformation. This confirms, as postulated in the Kolmogorov–Hinze theory, that breakup is essentially controlled by turbulent structures whose sizes are close to the bubble diameter. Moreover, the number of fragments depended on the specific shape of the bubble during the deformation process and varied in a wide range. Most of the time, two fragments were obtained (48% of cases), or between 3 to 10 (37%). Rarely more than 10 fragments (15%) were observed.

5. Determination of the critical Weber number

The dimensionless group which characterizes the deformation is the Weber number given by the Kolmogorov–Hinze theory,

$$We = \frac{\rho\,\overline{\delta u^2(d)}\,d}{\sigma}. \tag{6}$$

It involves the second-order longitudinal structure function expressed at a separation equal to the bubble diameter d,

$$\overline{\delta u^2(d)} = \overline{[u_z(z+d) - u_z(z)]^2}. \tag{7}$$

If the diameter d belongs to the inertial turbulent subrange, $\overline{\delta u^2(d)}$ may be expressed as a function of the dissipation rate ε:

$$\overline{\delta u^2(d)} = C(\varepsilon d)^{2/3}. \tag{8}$$

The relation between the constant C and the Kolmogorov constant C_k is found by integrating the turbulence spectrum,

$$C = \tfrac{27}{55}\,\Gamma(\tfrac{1}{3})\,C_k. \tag{9}$$

The calculation is identical to that of Batchelor (1953, p. 120), but here a one-dimensional instead of the three-dimensional spectrum is used. Putting $C_k = 1.5$ yields $C \sim 2$, and the classical expression proposed by Hinze (1955) follows:

$$We = \frac{2\rho\varepsilon^{2/3}\,d^{5/3}}{\sigma}. \tag{10}$$

The above formula clearly shows the dependence of the Weber number upon the bubble diameter.

In the present study, we propose to use directly the structure function $\overline{\delta u^2(d)}$ to avoid any assumption about the turbulence structure. The longitudinal velocity correlation coefficient $B_{zz}(d)$ was experimentally determined from simultaneous two-point measurements,

$$B_{zz}(d) = \frac{\overline{u_z(z)\,u_z(z+d)}}{(\overline{u_z^2(z)}\,\overline{u_z^2(z+d)})^{1/2}}. \tag{11}$$

In spite of the inhomogeneous character of the turbulence in the longitudinal direction, this coefficient remains independent of the z-coordinate (Risso & Fibre 1997). Hence, three effects can be distinguished in the expression for the structure function $\overline{\delta u^2(d)}$:

$$\overline{\delta u^2(d)} = \overline{u_z^2(z)}\left(1 + \frac{\overline{u_z^2(z+d)}}{\overline{u_z^2(z)}} - 2\left(\frac{\overline{u_z^2(z+d)}}{\overline{u_z^2(z)}}\right)^{1/2} B_{zz}(d)\right). \tag{12}$$

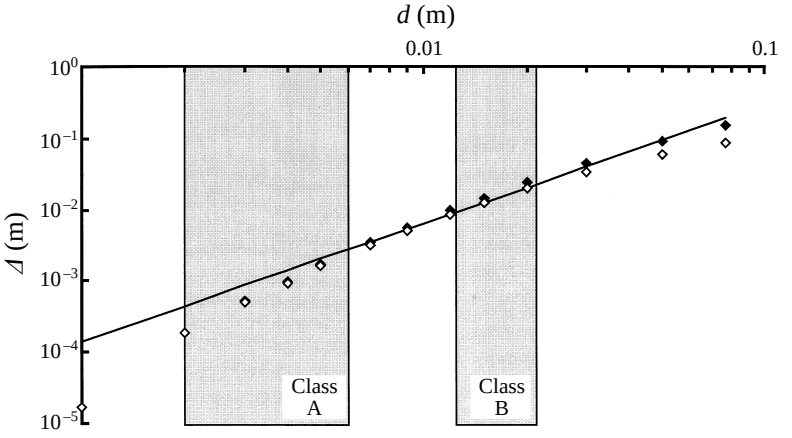

FIGURE 5. Weber number dependence upon the bubble diameter (the grey zones represent the diameter ranges of Classes *A* and *B*): ◆, Δ_{hom} (homogeneous approximation (14)); ◇, Δ (actual value, (15)); −, Δ_{fit} (−5/3 law fit, (16)).

The factor $\overline{u_z^2(z)}$ stands for the turbulence intensity. The correlation coefficient $B_{zz}(d)$ selects the amount of turbulent energy available at the bubble scale. Finally, the ratio of the fluctuations at the two location z and $z+d$ permits the inhomogeneity to be taken into account. To clarify the role of the bubble diameter, we define the function $\Delta(d)$ in such a way that the Weber number reads

$$We = \frac{\rho\,\overline{u_z^2(z)}\,\Delta(d)}{\sigma}. \tag{13}$$

If we neglect the inhomogeneity by setting to 1 the ratio of fluctuations in (12), it yields

$$\Delta_{hom}(d) = 2\,[1 - B_{zz}(d)]\,d. \tag{14}$$

Whereas, if we take into account the exponential decay of turbulence with z (1), we find

$$\Delta(d) = [1 + \mathrm{e}^{-2d/D} - 2\,\mathrm{e}^{-d/D}\,B_{zz}(d)]\,d. \tag{15}$$

Figure 5 shows the dependence of the Weber number upon the bubble diameter. For clarity, the ranges of bubble diameters are represented by grey zones. These results were obtained from the measurements of longitudinal velocity correlation coefficient. The homogeneous case ((14): filled diamonds) is compared to the inhomogeneous case ((15): open diamonds) and to the best fit of the classical 5/3 power law (line):

$$\Delta_{fit}(d) = 2.51 D (d/D)^{5/3}. \tag{16}$$

There exists a large range of bubble diameters where the classical law correctly fits the experimental results, whether inhomogeneity is taken into account or not. This proves that the largest bubble of class A and all the bubbles of class B belong to the inertial subrange. The substitution of the fit given by (16) into (13) leads to the following expression for the Weber number,†

$$We = 2.51\ (d/D)^{2/3}\,\frac{\rho\,\overline{u_z^2(z)}\,d}{\sigma}, \tag{17}$$

† The tube diameter D appears in (15), (16) and (17) because it is the relevant length scale in the present experiment. The exponential decaying length scale L and the longitudinal integral scale Λ are $L = 1.0D$ and $\Lambda = 0.27D$ respectively.

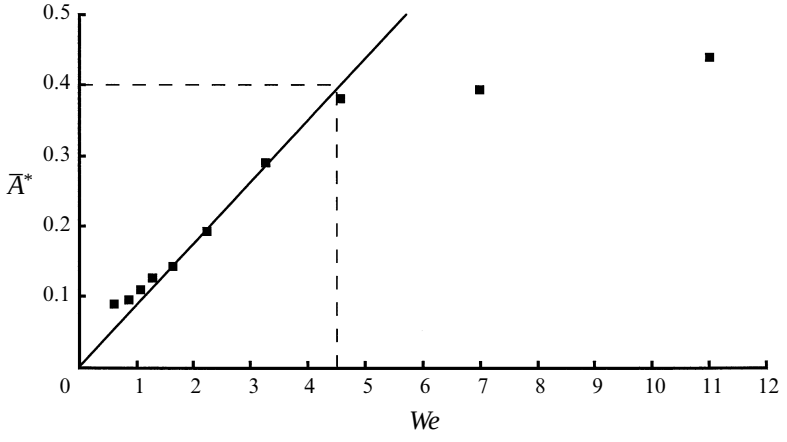

FIGURE 6. Experimental relation between mean deformation and mean turbulence intensity.

with a maximum error of 5% for class B bubbles and 20% for a bubble of 3 mm diameter. For our particular flow condition (17) is equivalent to (10). Thus, the results of the present study can be compared to those of authors who defined the Weber number by using (10) instead of (6).

The comparison of the results obtained for the two classes of bubbles shows that, in the test section, breakup occurred when the diameter was larger than 12.4 mm but did not when the diameter was less than 6 mm. This confirms the existence of a critical Weber number that can be estimated as follows. As the turbulence is not homogeneous in the test section, the maximum intensity, $\overline{u_z^2(z)}_{max} = 0.063\ \mathrm{m^2\ s^{-2}}$, experienced by the bubbles will be used in (13). Thus from experimental results the critical Weber number ranges between 2.7 and 7.8.

It is interesting now to look for a relation between the local mean turbulence intensity and the mean bubble deformation. In this respect, an Eulerian statistical approach was used. The test section was divided in the longitudinal direction into layers 10 mm thick. For each bubble belonging to class B, the projected area A^* and the axial location G_z were measured 125 times per second. All these samples were sorted with respect to their location G_z, whatever run they belong to. Then, the average value $\overline{A^*(z)}$ was determined for each layer. The number of samples available for averaging ranged between 200 to 900 depending on the layer. At each cross-section there was a corresponding turbulence intensity $\overline{u_z^2(z)}$. By eliminating the z-coordinate, a relationship between the turbulence intensity and the mean deformation was obtained. This is plotted in dimensionless form in figure 6 by using the average bubble diameter of class B, $d_{avg} = 18$ mm, to determine the Weber number (equation (13)). For a Weber number less than 4.5, the mean deformation $\overline{A^*}$ depends linearly on the Weber number and remains smaller than 0.4. The existence of a large linear domain for the bubble deformation is very remarkable. Even if this result was obtained for averaged quantities, it can be reasonably assumed that the linear behaviour exists also for instantaneous deformations. Moreover, the linear limit of $\overline{A^*} = 0.4$ is close to the minimum deformation $\overline{A^*} = 0.5$ beyond which breakup was observed. The limit of validity of the linear theory of deformation is thus very close to the breakup limit. This suggests that the linear theory is relevant in predicting the evolution of the bubble shape in turbulent flows up to the beginning of the breakup process. In addition, the critical Weber number can be expected to be close to the limit of linearity.

In the foregoing discussion the critical Weber number was estimated in two different ways. By investigating the behaviour of bubbles of different diameters, it was found to range between 2.7 and 7.8. Then, by analysing how the mean deformation related to the mean turbulence intensity, a value close to 4.5 was obtained. These two analyses suggest that, when the turbulence is the only cause of deformation, a minimal Weber number of about 5 is necessary for breakup. Let us compare this to previous studies performed in more complex flow conditions. Senhaji (1993) studied air bubbles in a uniform turbulent downflow. In his experiment the mean liquid velocity ($U \approx 0.3\ \mathrm{m\ s^{-1}}$) was chosen such that the drag force exerted on the bubble balances the buoyancy force. The turbulence was generated by an upstream oscillating grid. Using (10), his results led to a critical Weber number of about 0.25. This value is much smaller than the value obtained in the present study under microgravity conditions. Why such a difference? Let $We_U = \rho U^2 d/\sigma$ be the Weber number based on the mean liquid velocity. In the experiment of Senhaji, $We_U = 6.5$. This value is large enough to cause a strong deformation of bubble but not to break it. The role of the turbulence is thus to supply the amount of energy lacking to obtain the breakup of this pre-deformed bubble. The turbulent critical value of 0.25 is only the measure of this amount of energy. Moreover, the fact that 0.25 is much smaller than the value obtained in microgravity strongly suggests that the deformation caused by the bubble drift significantly contributed to the breakup. Hence, the correct breakup criterion should take into account We and We_U based respectively on the turbulence level and on the mean velocity. Sevik & Park (1973) studied the phenomenon for bubbles injected in the axis of a turbulent upward jet. They demonstrated the existence of a critical Weber number of about 2.5, which is less than that obtained in the present study. This also suggests that, in the jet experiment, the turbulence was not the single cause of bubble deformation.

6. Analysis of instantaneous deformations

In the previous section, we considered only the relationship between mean deformation and mean turbulent intensity. Although this approach allows us to quantify the turbulence level necessary for the breakup, it does not provide any insights into the deformation mechanism. We shall now focus on the instantaneous deformations with the aim of understanding how the bubble dynamics is driven by the turbulence of the continuous phase. The bubble may be considered as a dynamical system, the turbulence acting as the input, the bubble deformation being the output. By comparing the bubble response to the turbulent excitation, the characteristics of the system may be identified. Unfortunately, it was not possible, for technical reasons, to perform simultaneous measurements of turbulence and bubble deformations. To overcome this difficulty, we proceeded in two steps. In a first step the whole history of bubble deformation was analysed from a set of significant runs. We looked for the signatures of the eigenmodes of deformation and attempted to infer both bubble dynamics and the nature of the simultaneous turbulent fluctuations. In a second step, numerical simulations were performed. Experimental turbulent signals were used to excite a fictitious bubble whose behaviour was controlled by a linear oscillator model.

6.1. *Experimental results*

Figure 7 displays the evolution of the projected area for the runs presented in figure 4. Due to the stochastic character of the turbulence, each run is different. Nevertheless, the bubble dynamics is expected to be the same in each case. Thus, it is reasonable to

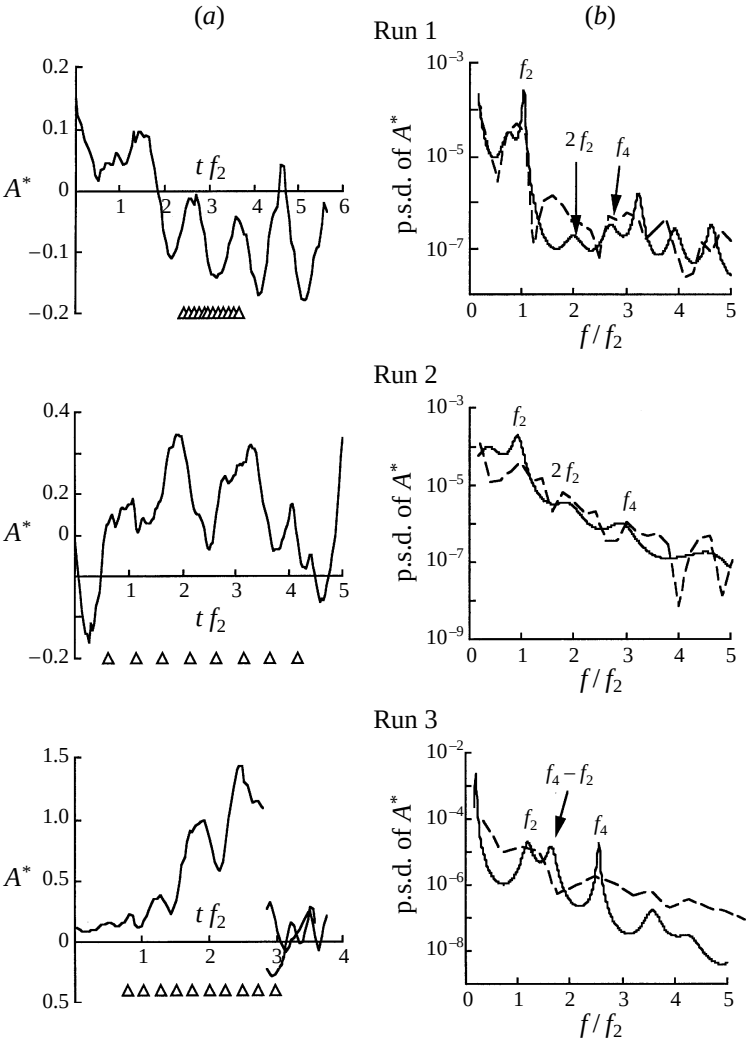

FIGURE 7. For caption see facing page.

try to identify its characteristic from individual realizations. With a view to detecting the signature of the eigenmodes of vibration (equations (3) and (4)), the power spectrum of the projected area is presented together with its time evolution.

Because of the short signal durations, about three to 10 times the period of the second mode, extraction of eigenfrequencies in the spectral plane is difficult. The periodogram method based on the fast Fourier transform is the most commonly used for obtaining power spectra. Unfortunately, its frequency resolution Δf is limited by the signal duration T_s,

$$\Delta f = c/T_s, \tag{18}$$

where c is a constant depending on the window function. In figure 7 the dashed lines represent the spectra obtained by this method: for runs 1–4, they show several peaks. But the signal to noise ratio and the resolution are too bad for an accurate determination of the corresponding frequencies. These uncertainties can be eliminated by the use of autoregressive methods (Kay & Marple 1981) whose resolution is not

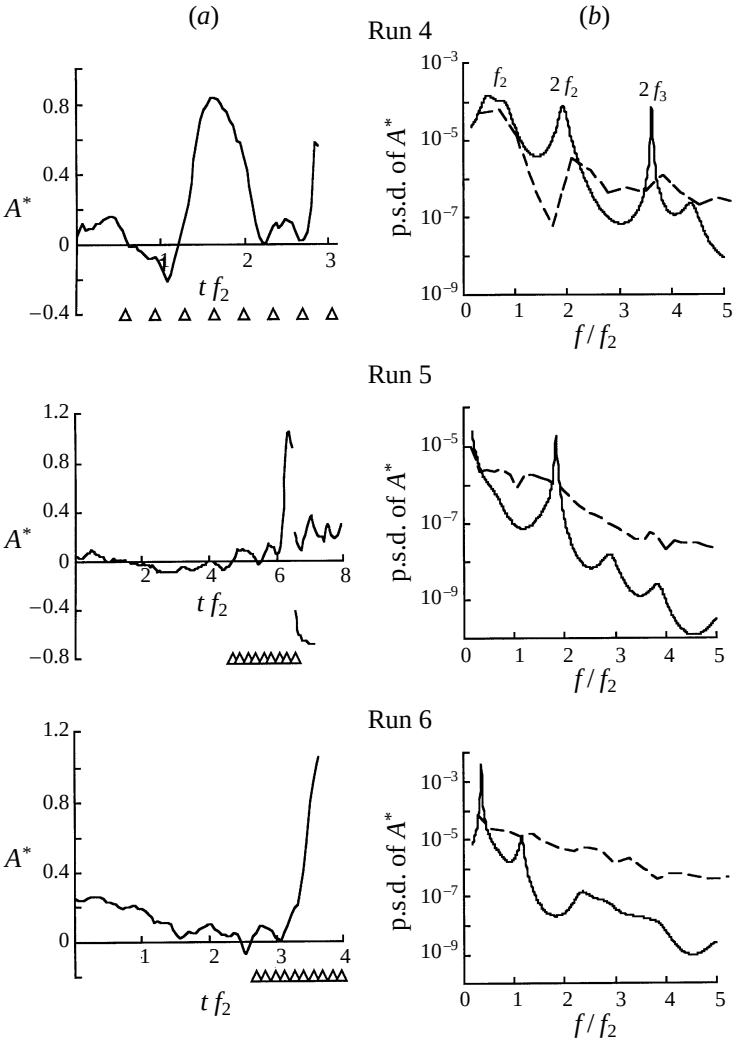

FIGURE 7. Measured deformations for the six runs pictured in figure 4: (*a*) time evolution of the relative projected area (Δ denotes the time instants corresponding to the pictures of figure 4); (*b*) power spectral density of the relative projected area (—, Fougere's method; ––, periodogram).

limited by the above criterion, (18). Here, we used Fougere's method (Chen 1982). It consists of modelling the signal samples by a linear filter. The coefficients of the filter are calculated by the use of an iterative procedure. The power spectrum can be expressed as an analytic function of these coefficients. In practice, the Fougere algorithm involves two arbitrary parameters; the number of iterations N_i, and the filter size N_f. The number of iterations has to be large enough for the method to converge: with 50 iterations the convergence was satisfactory. The filter characteristic results from a compromise: the greater its size, the better its resolution. But if it is too large, spurious peaks may appear from noise amplification or splitting of actual peaks. Three difference filter sizes ($N_f = 20$, 30 and 40) were tested with very similar results. However the filter size $N_f = 30$ provided a slightly better compromise: it was thus used for the results presented here (solid lines in figure 7). The advantage of the Fougere method is to clearly show the dominant frequencies of a signal (runs 1–4). But, we have to be

careful in cases of strong unsteadiness as for runs 5 and 6. Indeed, the peaks which appear in these situations do not correspond to any actual dominant frequencies.

Let us now return to the description of the physics. From observations covering fifty runs, three typical situations can be distinguished. In the first category (runs 1 and 2) the bubble was subject to oscillations of small amplitude and breakup never occurred. In the second category (runs 3 and 4), the bubble underwent several oscillations of large amplitude and generally split. The third category (runs 5 and 6) corresponds to sudden breakup without significant previous deformation.

First category: weak deformations (runs 1 and 2: figures 4 and 7) During run 1, the deformation remained very weak ($A^* < 0.2$). A careful inspection of the pictures (figure 4) shows a succession of lengthening–flattening cycles that is characteristic of the second eigenmode. The presence of this mode is confirmed by the evolution of the projected area in figure 7 where the main oscillations are distinctly visible at the frequency f_2. In the spectrum, the principal peak corresponds to the frequency f_2 (with a weak harmonics at $2f_2$). However, the signature of the fourth mode is also present (peak at f_4). Run 2 features similar behaviour although with a larger amplitude of oscillations ($A^* \sim 0.4$). The pictures show that the bubble has shapes similar to those predicted by the linear theory in spherical harmonics (see Trinh, Zwern & Wang 1982, for comparison). In particular, the first picture shows a triangular shape, typical of the third eigenmode. During the sequence, the succession of lengthenings and flattenings, typical of the second mode, is again present. In the time evolution of figure 7, oscillations at the frequency f_2 are now combined with oscillations at higher frequencies. The spectrum shows a dominant peak at the frequency f_2, and two minor peaks at $2f_2$ and f_4. From the pictures, a peak at $2f_3$ corresponding to the presence of the third mode can be expected. But, as shown in §3, the projection attenuates much more the energy of odd rather than of even modes.

All the bubbles undergoing deformations of small amplitude ($A^* \leqslant 0.4$) featured similar behaviour. The signatures of the eigenmodes of the linear theory were distinctly visible, the second mode being always dominant. Thus, it may be reasonable assumed that during these runs, the instantaneous turbulence remained weak in the vicinity of the bubble. Thus, the bubble is essentially driven by its own dynamics when it experiences a weak excitation.

Second category: complex evolutions (runs 3 and 4: figures 4 and 7) Run 3 (figure 7) is very different from runs 1 and 2 although oscillations were also present. Initially moderate, the bubble oscillations increased regularly with time.† Finally, the deformation became very large ($A^* \sim 1.5$) and breakup occurred. In the spectrum, the presence of second and fourth eigenmodes was shown by the peaks at $f_2, f_4 - f_2$, and f_4. Run 4 (figure 7) shows a different behaviour. At first, the bubble performed one complete lengthening–flattening cycle (second mode) of weak amplitude ($A^* \sim 0.2$). Then, it underwent a second cycle having a much larger amplitude ($A^* \sim 0.9$) before returning close to its equilibrium position. Finally, the deformation suddenly increased and breakup occurred. In the spectral plane, the signatures of eigenmodes are also visible. The peaks at f_2 and $2f_2$ prove the presence of the second mode, and the peak at $2f_3$ that of the third mode.

In this scenario, it is reasonable to believe that significant turbulent eddies were present in the vicinity of the bubble. In run 3, a constructive interaction between these turbulent structures and the bubble dynamics takes place. The bubble accumulates

† Note that the measured deformation determined from the relative projected area (equation (2)) may remain positive during oscillations of large amplitude (figure 7). This is an artefact due to the projection.

energy of deformation and finally breaks up. For run 4, it is likely that a first turbulent eddy caused a large deformation. However it did not contain enough energy to cause breakup. During the following oscillation the bubble lost almost all its energy of deformation. This is probably due to a destructive interaction between turbulence and bubble dynamics. At the end, another significant eddy occurred and caused the breakup.

In these situations, the turbulence and the bubble dynamics seem to interact in a complex way to control the deformation. The bubble shape depends not only on the instantaneous turbulence level in the neighbourhood of the bubble, but also on the entire history of turbulence and deformation. Indeed, if the arrival of a turbulent eddy is in phase with the bubble oscillations the deformation increases (constructive interaction), otherwise it may decrease (destructive interaction).

Third category: Sudden breakup (runs 5 and 6: figures 4 and 7) Runs of the third category are the most likely to lead to breakup. This is illustrated by the two last examples (runs 5 and 6). An initially non-deformed bubble suddenly underwent a very large deformation ($A^* > 1$). Then, it split without having performed any significant oscillations. Observation of the projected area (figure 7) shows that it is useless to try to find the signature of the eigenmodes (spectra are just presented here for comparison between the periodogram algorithm and the Fougere's method). In these situations, the evolution of the bubble shape exhibited two stages. At first, the turbulence intensity near the bubble was probably weak and the deformation remained moderate. Then it is likely that the bubble encountered a turbulent eddy intense enough to cause breakup. Depending on the exact characteristics of this eddy the breakup process may differ. Indeed, while run 5 shows a lengthened bubble which broke into two parts, run 6 displays a flattened bubble which split into a swarm of small fragments. But in both cases, the deformation seems to be controlled by the action of a single eddy. The corresponding breakup process is independent of the turbulence history.

6.2. *Simulations*

The experimental results have confirmed the importance of bubble dynamics in the deformation process. To verify this idea, numerical simulations of the bubble response to the turbulent excitation were performed. This suggests the introduction of a dynamical model L for the bubble and the use of an input signal $F_{ex}(t)$ having the correct turbulence characteristics.

Let us discuss the dynamical model. Experiments have shown that the second eigenmode of oscillation is largely predominant. Furthermore, the linear limit found in §5 from figure 6 ($A^* = 0.4$, $We = 4.5$) suggests that the linear theory is probably valid up to the breakup limit. Consequently, we propose to use the linear model of Lamb (1932) for the oscillation of a bubble in a viscous fluid,

$$L(r) = \frac{\mathrm{d}^2 r}{\mathrm{d}t^2} + \frac{2}{\tau}\frac{\mathrm{d}r}{\mathrm{d}t} + 4\pi^2 f_2^2 r, \tag{19}$$

where r is the deformed radius of the bubble, f_2 (equation (4)) and τ are the frequency and the damping time of the second mode. This damping time depends on the kinematic viscosity of the continuous phase ν and on the non-deformed bubble diameter d:

$$\tau = \frac{1}{80}\frac{d^2}{\nu}. \tag{20}$$

Equation (19) considers only the second eigenmode of vibration. The bubble shape is thereby reduced to a scalar function of time.

Now, the turbulence excitation has to be modelled. Regarding the role of the different turbulent scales, the same assumption as in the Kolmogorov–Hinze theory (see §5) can be applied to instantaneous fluctuations. The turbulence forcing may be expressed as

$$F_{ex}(t) = Kd\delta u^2(d,t), \tag{21}$$

where K is a dimensionless constant of order 1. Unfortunately, the time resolution of our two-point measurements does not allow us to use (21) directly. An additional assumption has been made to relate the instantaneous squared velocity difference $\delta u^2(d,t)$ to the instantaneous squared velocity fluctuation $u_z^2(z,t)$: the relationship between their mean values is assumed to apply to their instantaneous values:

$$\delta u^2(d,t) \approx \frac{\overline{\delta u^2(d)}}{\overline{u_z^2(z)}} u_z^2(z,t) = \frac{\Delta(d)}{d} u_z^2(z,t), \tag{22}$$

where $\Delta(d)$ is the function introduced in §5 and plotted in figure 5. The ratio $\Delta(d)/d$ acts as a spatial filter. It guarantees that only the amount of turbulent energy available at the bubble scale is taken into account. This formulation allows the separation of the time evolution of the turbulence from its spatial structure.

All quantities will be hereafter denoted by a star and normalized by using the period of oscillation $(1/f_2)$ as a time scale and the bubble diameter d as a length scale. Using the dynamical model given by (19) and the turbulence excitation modelled by (21) and (22), yields

$$\frac{\mathrm{d}^2 r^*}{\mathrm{d}t^{*2}} + 2\xi \frac{\mathrm{d}r^*}{\mathrm{d}t^*} + r^* = K'\, We(t^*) \tag{23}$$

where $\xi = 1/(2\pi\tau f_2)$ is the damping coefficient of the oscillator. In the case of an air bubble in water, ξ is much less than unity ($\xi = 0.007$ for $d = 18$ mm). The expression for the Weber number is the same as in (13) except that the instantaneous fluctuation is used here:

$$We = \frac{\rho u_z^2(t)\,\Delta(d)}{\sigma}. \tag{24}$$

Numerical simulations of (23) have been performed. The initial condition corresponds to a bubble at rest ($r^* = \mathrm{d}r^*/\mathrm{d}t^* = 0$). For the Weber number $We(t)$, an experimental turbulence signal $u_z^2(t^*)$ obtained by laser doppler anemometry was used. It was measured at the tube axis in the middle of the turbulent test section ($z = 350$ mm) where the standard deviation $\overline{u_z^2}^{1/2}$ was equal to 0.1 m s^{-1}. The total signal duration was 1000 s with a mean sampling rate of about 50 samples per second. To ensure sufficient accuracy in solving (23), the signal was resampled at 1000 Hz by use of the generalized Shannon method (Veynante & Candel 1988). A numerical integration was then performed using the Runge–Kutta–Nyström algorithm (Nyström 1925), which is a fourth-order-accurate scheme. The order-1 constant K' was set to 1, which will be justified below from quantitative comparisons with experimental results. It is worth nothing that the turbulence signal was obtained in the absence of a bubble, thus our model neglects possible distortions of the turbulence by the interface.

Our first objective was to perform qualitative comparisons between simulations and experiments. For this purpose, the first 100 s of the signal was divided into one hundred samples of 1 s duration. The response of a bubble of 18 mm diameter (mean bubble diameter of class B) to each of these turbulent realizations was computed. These simulations display characteristics similar to the experiments. In particular, three identical categories of behaviour can be distinguished. For illustration, four typical

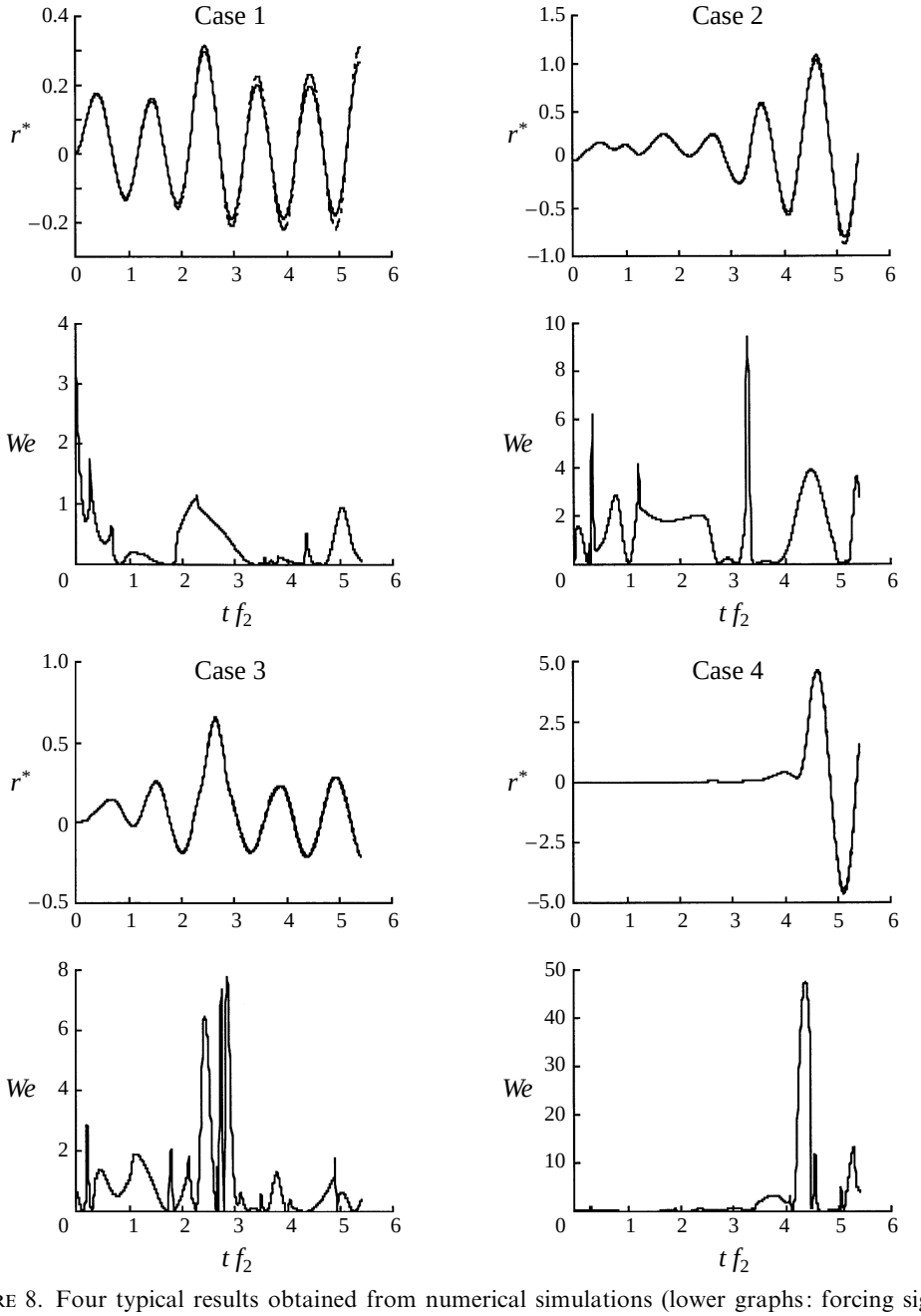

FIGURE 8. Four typical results obtained from numerical simulations (lower graphs: forcing signal $We(t)$; upper graphs: simulated deformation). Dashed line: same simulations but with zero damping coefficient.

runs are presented in figure 8. The numerical simulations have the great advantage over the experiments of presenting simultaneously the turbulence excitation and the resulting deformation. Consequently, the three categories of run can be analysed in order to shed light on the energetic role of turbulence.

First category: weak turbulence ($We < 3$) Case 1 (figure 8) is similar to experimental runs 1 and 2. The bubble oscillates in turbulence of weak intensity. The

Weber number remains less than 2 and the amplitude of the deformation never exceeds 0.4. It must be recalled that only the second mode is present in the numerical simulations so that the time evolution of the calculated deformation is smoother than the measured one. Nevertheless the conclusion remains the same as for the experiments: when the instantaneous turbulence is weak, the deformation is essentially controlled by the bubble dynamics.

Second category: succession of moderate turbulent eddies ($We < 10$) Cases 2 and 3 (figure 8) correspond to complex evolution of the bubble shape which occurs when turbulence and bubble dynamics combine their effect. In these two cases, several moderate turbulent eddies ($3 < We < 10$) successively appear. Case 2 is analogous to experimental run 3 (figure 7). Each turbulent eddy alone is not capable of causing large deformation, but their succession interacts in a constructive way with the bubble dynamics. The bubble accumulates energy and finally undergoes a deformation large enough to break it. Case 3 (figure 8) is similar to the experimental run 4 (figure 7). Three eddies containing moderate energy ($6 < We < 8$) appear during one period of oscillation. The first increases the deformation whereas the two others are out-of-phase with the bubble oscillations and decrease the deformation. It should be pointed out that this decrease is due to a destructive interaction and not to some dissipative effect. To confirm this argument, identical simulations have been performed with a zero damping coefficient ($\xi = 0$). The corresponding results are represented in figure 8 by dashed lines. For such a short simulation time, damping is negligible. Thus the following conclusion may be drawn from both physical and numerical experiments: when the excitation is due to eddies of moderate energy, their time succession plays a major role in the breakup process.

Third category: single intense eddy ($We > 10$) Case 4 (figure 8) is similar to experimental runs 5 and 6 (figure 7). A single intense turbulence eddy ($We \sim 50$) may be responsible for large deformation of an initially non-deformed bubble. In the numerical simulations, no breakup criterion was introduced. Hence, the bubble is subjected to an oscillation of huge amplitude. In such a situation, experimental results show that breakup occurs. In contrast to the previous cases, the history of deformation does not play any role. The entire process is controlled by the energy of a single intense eddy.

The agreement between physical and numerical experiments suggests a twofold conclusion. First, the complexity of the problem lies mainly in the stochastic succession of turbulent eddies. Secondly, the simple linear oscillator exhibits the main characteristics of the bubble dynamics.

Is it possible to improve this model by taking into account the nonlinear effect of large deformation? The only nonlinear model available today is due to Kang & Leal (1990). By using the relationship between the Weber number and the steady shape of a bubble in a steady uniaxial straining flow, the authors inferred a nonlinear correction (23):

$$\frac{\mathrm{d}^2 r^*}{\mathrm{d}t^{*2}} + 2\xi \frac{\mathrm{d}r^*}{\mathrm{d}t^*} + \left(1 - \frac{r^*}{2r_c^*}\right) r^* = K' We(t^*), \tag{25}$$

where r_c^* is the maximum stable deformation in the corresponding steady flow. This model was developed to study the resonant breakup of a bubble in an axisymmetric straining flow, periodic with time. Unfortunately, it did not provide satisfactory results in the present turbulent situation. In contrast to the linear parameters (natural frequency and damping time), the critical deformation r_c^* is not universal: it depends on the flow structure. In turbulent experiments the flow around the bubble is never the

same. Thus the value of r_c^* varies and the prediction of the model is not correct. In fact, the present modelling is based on two assumptions. The first is the linear approximation. The second consists in reducing the description of turbulence and bubble shape with space and time to the time evolution of a scalar parameter. The limit of validity of these two hypotheses is nearly the same, close to the breakup limit. Therefore, it is inconsistent to improve the present model for large deformations by considering nonlinear effects without taking into account the spatial character of both turbulence and bubble deformation.

6.3. *Conclusion about the breakup mechanism*

The analysis of instantaneous deformations shows that for a given turbulence intensity, two processes can lead to the breakup. The first involves an interaction between the bubble dynamics and the stochastic succession of turbulent eddies. Depending on the time arrival of turbulent eddies during each cycle of bubble oscillation, the deformation may increase or decrease. When it increases, the bubble may accumulate enough energy to break: this is a resonance-like mechanism that strongly depends on the entire history of turbulence and deformation. The second process is simpler. There exist turbulent eddies intense enough to cause the sudden breakup of an initially non-deformed bubble. In this situation, large deformations can be reached without any previous oscillations. This mechanism is independent of the history of deformation. It depends only on the instantaneous level of turbulence and can be interpreted through a simple force balance. For our experimental conditions – residence time ≈ 1 s, standard deviation of velocity ~ 0.3 m s^{-1} – the second mechanism was more frequently encountered than the first one.

7. Statistics of deformation

7.1. *Definitions of statistical tools*

In §6, it was shown that the numerical simulations present the features that were observed in the experiments. But even if the amplitudes of deformation that were predicted for each category of runs have the correct order of magnitude, the comparisons remain essentially qualitative. To make these comparisons quantitative, the statistics of deformation must be used.

Let us consider an initially non-deformed bubble which is put into the turbulent field at $t = 0$. We define $\zeta(t)$ as the maximum deformation experienced by the bubble within the interval $[0, t]$,

$$\zeta(t) = \max_{[0,t]}(r^*). \tag{26}$$

The statistics of the stochastic variable $\zeta(t)$ are entirely determined by the distribution function F_t which is the probability that the maximum deformation $\zeta(t)$ is less than Z,

$$F_t^d(Z) = \mathrm{Prob}(\zeta(t) \leqslant Z). \tag{27}$$

This function increases from zero to one when Z varies from zero to infinity. It can be estimated from both experimental and numerical results.

Let us consider the numerical simulations carried out with the experimental excitation $We(t)$. This signal extended over 1000 s and was divided into N samples of duration t. For each sample, the response of a 18 mm bubble was computed from (23) and the maximum deformation $\zeta(t)$ was determined. Then, the distribution function $F_t(Z)$ was obtained. To reveal the role of the damping, the same calculations were made by setting to zero the damping coefficient ξ: the resulting computed distribution

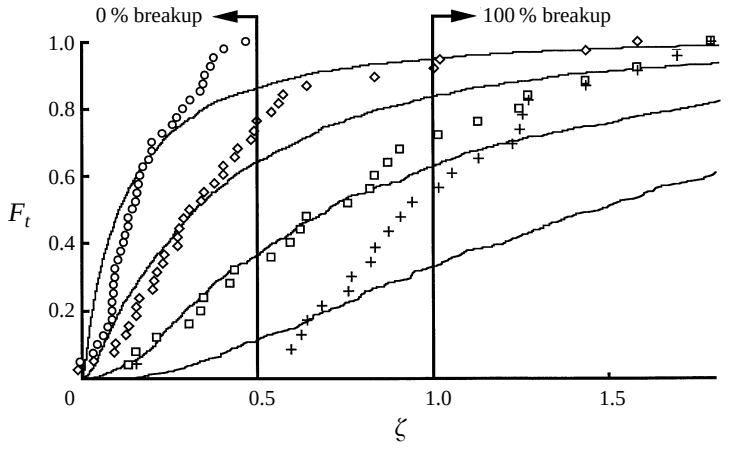

FIGURE 9. Statistics of the maximum deformation for four different residence times: experimental results (F_t^{exp}) ○, $t = 0.25$ s; ◇, $t = 0.5$ s; □, $t = 1$ s; +, $t = 2$ s; and −, corresponding numerical simulations (F_t^a).

function will be called F_t^{nd}. Let us define in a similar way the distribution function F_t^{turb} of the maximum turbulence intensity, that can be determined from the excitation signal $We(t)$:

$$F_t^{turb}(Z) = \text{Prob}\,(\max_{[0,t]}(We) \leqslant Z). \tag{28}$$

Let us consider now the experiments. Special care must be taken in estimating the distribution function F_t^{exp} of the maximum deformation. Indeed, in some cases the initial bubble deformation was not negligible. Thus, we have rejected the runs in which the initial projected area $A^*(t = 0)$ was greater than 0.1. As a consequence, only 40 among the 53 runs of class B were retained for the statistics. F_t^{exp} was obtained by determining the maximum deformation over the interval starting at the time when the bubble entered the test section and ending at time t or at the breakup time. (Note that since the experimental deformation is obtained from the bubble projected area, r^* has to be replaced by A^* in (26).) In addition, as experiment durations are not the same, the greater t, the fewer results are available. This point is however of minor importance since for large t breakup is expected to occur and the numerical simulations become questionable.

7.2. *Comparisons between simulations and experiments*

Figure 9 shows the experimental and numerical distribution functions of the maximum deformation for four different residence times, namely, $t = 0.25$, 0.5, 1 and 2 s. Symbols correspond to experimental results and curves to simulations. The two vertical lines represent the experimental breakup limits. When the maximum deformation ζ remains less than 0.5, breakup never occurs. When it exceeds 1, it always occurs after a certain time.

There exist two significant differences between simulations and experiments. The first concerns the shortest residence time ($t = 0.25$ s). For deformations larger than $\zeta = 0.3$ (20 % of cases), the simulations and experiments significantly differ. For short time experiments, the bubble was most of the time in the weak turbulent region (it must be kept in mind that the turbulence is inhomogeneous). Thus, the probability for the bubble to encounter intense turbulent eddies has been overestimated in the numerical simulations because the turbulent intensity corresponding to the middle of the

turbulent zone was used. Hence for short residence times, the simulations predict larger deformations than those observed in the experiments. This drawback is considerably reduced for larger residence time since the bubble travels over the entire test section. The second difference concerns large deformations. Beyond $\zeta = 0.5$, breakup becomes possible. Thus, as no breakup criterion was introduced, the simulations predict unrealistic deformations corresponding to situations in which breakup actually occurs. Nevertheless, the simulations provide very good results up to $\zeta = 0.5$ for a residence time of 0.5 s, and even up to $\zeta = 0.8$ for $t = 1$ s. For a residence time of 2 s, almost all the deformations exceed the limit of possible breakup ($\zeta = 0.5$), and 50 % exceed the limit of inevitable breakup ($\zeta = 1$). In this situation, the simulations are not relevant because the linear assumption does not hold anymore.

In spite of the small number of available experiments (40), the use of the projected area to measure the deformation and the inhomogeneity of the turbulence field, the quantitative agreement between experiments and simulations is remarkable. The use of the linear model in which the single adjustable constant K' has been set to unity is thus legitimated for describing the bubble behaviour up to the breakup limit ($\zeta = 0.5$).

The fundamental conclusion arising from the results presented in figure 9 is the strong dependence of the statistics of deformation upon the residence time. The results of §6 show that the amplitude of deformation increases with time for two reasons. The first is related to the possibility that the bubble can extract energy from successive turbulent eddies and retain it in its oscillatory deformation. The longer the time during which the bubble remains in the turbulence field, the greater the probability it accumulates a large amount of energy. The second reason lies in the fact that the probability of encountering intense turbulent eddies increases with the time of residence. These two mechanisms must be combined to predict the breakup probability. In the previous section, it was shown that these two mechanisms are well reproduced by the linear model from a qualitative point of view. In this section, we found that it is able to predict quantitatively the statistics of bubble deformation from the statistics of turbulence.

7.3. *Role of the bubble dynamics*

The preceding results authorize a more systematic use of numerical simulations to investigate the role of the bubble dynamics in the deformation process. Let us discuss first the conditions for which the breakup mechanism results from a simple force balance. In previous studies, the role of the succession of turbulent eddies is often neglected. Delichatsios (1975) tried to determine the limit of validity of this assumption. He proposed a comparison of the bubble response time $1/f_2$ to the characteristic time of a turbulent eddy $d^{2/3}/\varepsilon^{1/3}$. He assumed that if the former is sufficiently shorter than the latter, the bubble dynamics do not play any role. Furthermore, he claimed that, in this situation, the probability of breakup is only controlled by the probability for the instantaneous turbulent intensity to exceed a given value. But this argument is inexact because it does not involve the correct time scales. Recently, Shreekumar, Kumar & Gandhi (1996) studied the bubble response to a single eddy and claimed that '[…] if a pressure fluctuation on the surface of the drop acts for the lifetime of an eddy that deforms it in some direction, it is unlikely that the next pressure fluctuation on the drop surface of the drop will act in a coherent manner to continue the deformation process' and concluded that 'Drop-eddy interactions occur in a random manner and not in any cooperative fashion'. The present study contradicts this assertion since we have shown that the bubble can accumulate (constructive interaction) or lose (destructive interaction) some energy during its interaction with a turbulent eddy. In fact, the energy must, on average, increase continuously with time as proved from the theory of

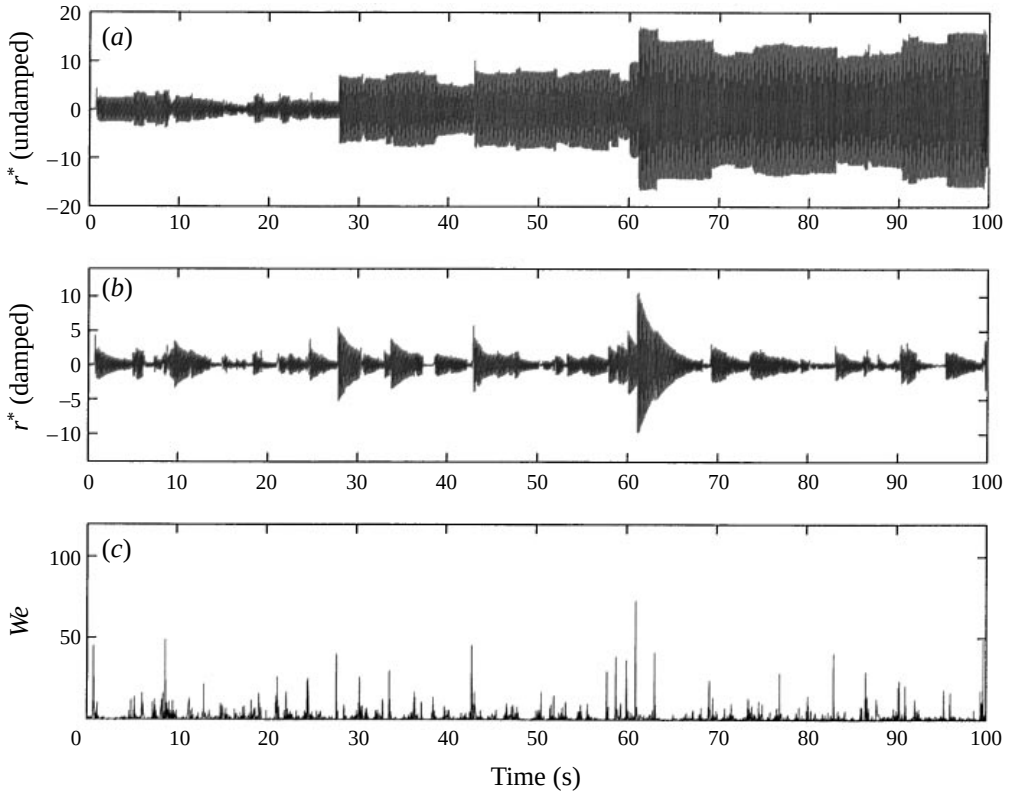

FIGURE 10. Comparison of damped and undamped simulations for a bubble of 14 mm diameter.

stochastic processes. If $\Phi(f)$ is the power spectral density† of the turbulent excitation $We(t)$, the variance $\overline{r^{*2}(t)}$ of the linear oscillator response (23) is then given by (Preumont 1990, p. 92)

$$\overline{r^{*2}(t)} = \frac{\Phi(f_2)}{16\pi^2 \xi f_2^3}(1-\mathrm{e}^{-4\pi\xi f_2 t}), \tag{29}$$

where f_2 is the natural frequency of the oblate–prolate surface mode defined in (4). For large times $\overline{r^{*2}(t)}$ tends to a finite limit which is inversely proportional to the damping coefficient ξ. If damping is neglected the variance is unbounded and increases linearly with time:

$$\overline{r^{*2}(t)} = \frac{\Phi(f_2)}{4\pi f_2^2} t. \tag{30}$$

Although the deformation process is essentially inertial, the viscous dissipation cannot be neglected for large residence times. This is illustrated in figure 10(*c*) with the response of a 14 mm diameter bubble subjected to a turbulent forcing of 100 s. The undamped case is plotted in figure 10(*a*): even if destructive interaction sometimes occurs, the deformation tends to increase. Figure 10(*b*) presents the damped simulation ($\xi = 0.008$): the damping causes the bubble to return to rest during the periods of weak turbulence. If the time elapsed between two eddies is large enough compared to the damping time τ, the bubble can never accumulate energy. Thus, the correct validity

† $\Phi(f)$ is not the classical velocity spectrum, it is the spectrum of the instantaneous Weber number involving the squared velocity.

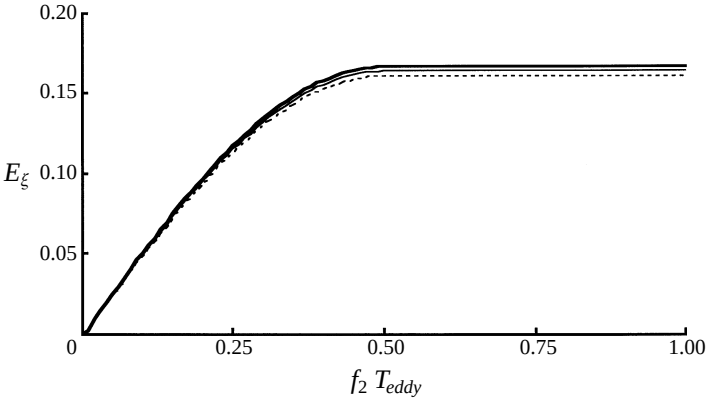

FIGURE 11. Efficiency of an isolated eddy of duration t in deforming the bubble: ——, $\xi = 0$ ($d \to \infty$); — —, $\xi = 0.01$ ($d = 10$ mm); – –, $\xi = 0.022$ ($d = 2$ mm).

criterion of the force balance interpretation involves the comparison between the damping time and a characteristic time of occurrence of intense turbulent eddies. We do not provide a precise definition of this time scale here. It is likely to be closely related to intermittence.

Once the mechanism of energy accumulation from a succession of turbulent eddies has been demonstrated, it is interesting to investigate the response of the bubble to an isolated eddy. Let us model a turbulent eddy as

$$\left.\begin{aligned} We(t) &= 0, && t < 0, \\ We(t) &= W_{eddy}, && 0 \leqslant t \leqslant T_{eddy}, \\ We(t) &= 0, && t > T_{eddy}, \end{aligned}\right\} \tag{31}$$

where W_{eddy} stands for its intensity, and T_{eddy} for its duration. The maximum deformation r^*_{max} of a bubble subjected to the forcing given by (31) is calculated by solving (23). It yields

$$r^*_{max} = W_{eddy}\, E_\xi(f_2\, T_{eddy}). \tag{32}$$

The function E_ξ represents the eddy efficiency. It is plotted in figure 11 for three different damping coefficients corresponding respectively to the smallest bubble of our experiments ($\xi = 0.022$), to a centimetric bubble ($\xi = 0.01$) and to the ideal undamped case ($\xi = 0$). When the eddy duration is less than half the natural bubble period, the efficiency E_ξ is an increasing function of the normalized eddy duration. Beyond $f_2\, T_{eddy} = 0.5$, the maximum efficiency is reached. This latter depends on the damping coefficient. But for bubbles in water with diameter greater than 2 mm, the difference with the undamped value ($= 1/6$) is negligible.

For our experimental conditions, the characteristic time of eddies ($d^{2/3}/\varepsilon^{1/3} \sim 0.25$ s for a 18 mm diameter bubble in the middle of the test section) is larger than half the bubble period ($1/f^2 \sim 0.19$ s). Nevertheless, it cannot be concluded that the efficiency is equal to $1/6$ for each eddy. Indeed, the turbulent signals presented in figure 8 show that the signature of eddy duration varies: it is close to $1/f_2$ for the longest, but is significantly shorter for the most intense eddies. Thus, the efficiency is a random variable, its average being expected to be less than $1/6$.

Now, the deformation process can be summarized. The turbulence acts as a succession of turbulent eddies with random time of arrival and intensity. The bubble

dynamics respond to this forcing by two distinct mechanisms. The first mechanism is related to the efficiency of each individual eddy which depends essentially on the ratio between the eddy duration and the bubble period. The second controls the accumulation of energy from successive eddies. It depends on the power available at the bubble natural frequency in the forcing signal $We(t)$ and on the ratio between the damping time and the time between two successive eddies.

7.4. *Influence of bubble size*

Let us now investigate the influence of bubble size. In the various studies related to turbulent breakup, the influence of the bubble diameter is very limited since it appears only in the expression for the Weber number (6). Because the diameter also controls the dynamical characteristics of the bubble – natural frequency f_2 (4), and damping time τ (20) – its importance must be wider. Indeed, restricting the influence of the bubble diameter to the Weber number is equivalent to assuming that the deformation process does not depend on the bubble dynamics. This should imply that the statistics of maximum deformation would have the same behaviour as the statistics of the maximum turbulent intensity. The comparison between these two behaviours for different bubble diameters is thus a way of investigating in detail the role of the bubble size.

Let us introduce the mean efficiency coefficient $C_d(t)$ as the ratio between the average of maximum deformation and the average of maximum Weber number:

$$C_d(t) = \int_0^\infty \zeta \, \mathrm{d}F_t \Big/ \int_0^\infty We \, \mathrm{d}F_t^{turb}. \tag{33}$$

Figure 12 shows F_t^d (thick line), F_t^{nd} (thin line) and F_t^{turb} (dashed line) for four different bubble diameters ($d = 8$, 13, 18 and 23 mm) and three different residence times ($t = 0.25$, 2 and 20 s).† For each bubble diameter, the turbulence distribution functions F_t^{turb} have been multiplied by the mean efficiency coefficient corresponding to the shortest available residence time: $C_0 = C_d$ (0.25 s).

For this residence time, the three distribution functions for the three bubble diameters cannot be distinguished from each other. Thus the residence time is not large enough for the damping or the energy accumulation process to be effective. The mechanism is controlled by inertia and the bubble deformation is driven by the response to individual eddies. Therefore, the analysis of §7.3 concerning individual eddies must apply. Indeed, as predicted by the result plotted in figure 11, the mean efficiency coefficient increases with the natural frequency f_2 and thus decreases with the bubble diameter:

$$\left.\begin{array}{lll} d = 8 \text{ mm}, & f_2 = 18.2, & C_0 = 0.11, \\ d = 13 \text{ mm}, & f_2 = 8.8, & C_0 = 0.084, \\ d = 18 \text{ mm}, & f_2 = 5.4, & C_0 = 0.062, \\ d = 23 \text{ mm}, & f_2 = 3.7, & C_0 = 0.043. \end{array}\right\} \tag{34}$$

Note that all the values of C_0 are smaller than the theoretical maximum of 1/6.

The statistics of deformation of the 8 mm bubble remains very close to the turbulence statistics even for a residence time of 20 s. The damping time ($\tau = 0.8$ s) is

† Deformations for large time are unrealistic since breakup finally occurs. But since a linear model is used, the relative evolution of the deformations with the residence time or bubble diameter is independent of the turbulence intensity.

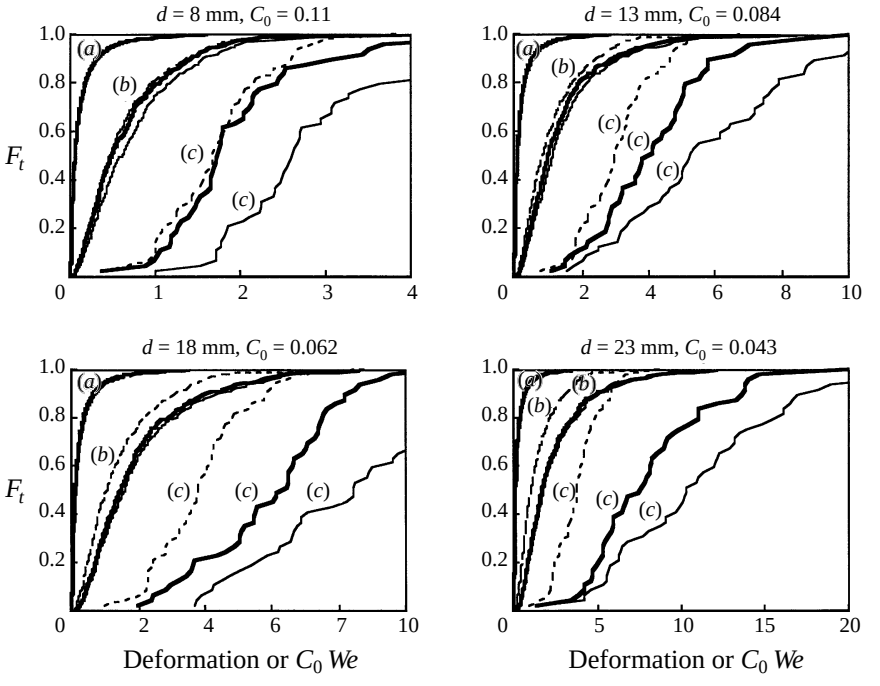

FIGURE 12. Simulated statistics of the maximum deformation (——, F_t^{nd}, ▬, F_t^{d}) and of the maximum Weber number (– –, F_t^{turb}) for four different bubble diameters and three residence times (*a*) $t = 0.25$ s, (*b*) $t = 2$ s, (*c*) $t = 20$ s.

short compared to the eddy separation. Therefore, the bubble can never accumulate energy and the maximum deformation results from the response to individual eddies. In this situation the force balance interpretation applies. For the 13 mm bubble ($\tau = 2.11$ s), the statistics of deformation slightly exceed the statistics of the turbulent excitation for $t = 2$ s. For $t = 20$ s, this difference is much greater, indicating that energy accumulation takes place. The two other graphs show that the larger the bubble, the greater the energy accumulated from successive eddies.

The role of the bubble diameter in the damping is shown in figure 12 through the comparison between damped and undamped cases. Since the damping coefficient is an decreasing function of the diameter, the difference between damped and undamped distribution functions decreases when the bubble size increases: for the largest bubbles the limitation of the energy accumulation by the damping (29) is visible only for $t = 20$ s, whereas it is visible as early as $t = 2$ s for the smallest one.

The above results are summarized in figure 13 (undamped case: open symbols, damped case: filled symbols) where the time evolution of the mean efficiency coefficient $C_d(t)$ is presented for the four diameters under investigation ($d = 8$ mm: circles, $d = 13$ mm: diamonds, $d = 18$ mm: squares, $d = 23$ mm: triangles). Since it has been normalized by the average maximum turbulent intensity, $C_d(t)$ is only representative of the energy accumulation process. If $C_d(t)$ is independent of the residence time, the deformation is strongly correlated to the turbulence excitation and does not depend on the history of this excitation. Then the deformation versus turbulence process results from a force balance. Figure 13 confirms that this is roughly the case for the smallest bubble. If the influence of the bubble diameter were restricted to its contribution to a force balance, then $C_d(t)$ would be independent of the bubble diameter. Figure 13

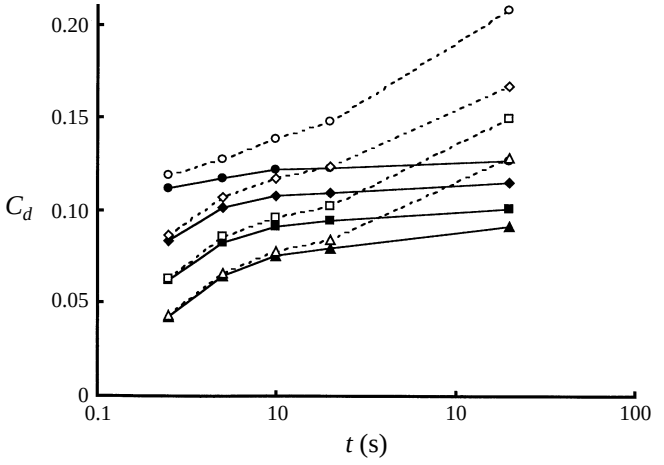

FIGURE 13. Evolution of the mean efficiency coefficient with the residence time for four different bubble diameters: ○, $d = 8$ mm (undamped); ◇, $d = 13$ mm (undamped); □, $d = 18$ mm (undamped); △, $d = 23$ mm (undamped); ●, $d = 8$ mm (damped), ◆, $d = 13$ mm (damped); ■, $d = 18$ mm (damped); ◆, $d = 23$ mm (damped).

shows that this is not true: $C_d(t)$ is a decreasing function of the bubble diameter even for the largest residence times. Consequently, it must be stressed that, for the same Weber number, the deformation of a small bubble is always greater than the deformation of a large bubble.

7.5. *Improvement of the Kolmogorov–Hinze theory*

The Weber number introduced by Kolmogorov and Hinze (6), is a relevant parameter to characterize the deformation of a bubble in a turbulent field. It can be interpreted as a measure of the amount of turbulent kinetic energy available at the bubble scale. However, it ignores the bubble response to a random turbulent excitation.

In fact, the bubble dynamics involves two time scales. The first is the period of the second eigenmode of vibration ($1/f_2$) that depends on both surface tension and bubble diameter. The second is the exponential damping time τ that varies with the viscosity of the continuous phase and the bubble diameter. To take into account the bubble dynamics, the mean efficiency coefficient $C_d(t)$, (33), was introduced. This coefficient is a function of the residence time of the bubble in the turbulent field. It takes into account two effects. The first concerns the bubble response to isolated eddies and thus imposes the value of C_d for short residence times, $C_d(t \to 0)$. The second is related to the accumulation of energy by the bubble from the stochastic turbulent excitation and it is responsible for the increase of C_d with time.

The Kolmogorov–Hinze theory may be improved by introducing the product of the Weber number and the mean efficiency coefficient $We\, C_d$. Three situations can be distinguished:

(i) The turbulence is weak, i.e. $We\, C_d(t \to \infty) <$ c.v., where c.v. is a critical value. Individual eddies are not capable of causing breakup and the accumulation of energy is not sufficient. Breakup is impossible.

(ii) The turbulence is moderate, i.e. $We\, C_d(t \to \infty) >$ c.v. and $We\, C_d(t \to 0) <$ c.v. Individual eddies are still not capable of breaking the bubble, although a succession of turbulent eddies may be. Breakup is controlled by a resonance-like mechanism.

(iii) The turbulence is intense, i.e. $We\, C_d(t \to 0) >$ c.v. Individual eddies are capable

of causing the sudden breakup of a previously non-deformed bubble. The corresponding breakup mechanism agrees with the force balance interpretation.

8. Conclusion

The present study provides several original quantitative and qualitative results concerning the deformation and breakup of bubbles by a turbulent field.

First, the Kolmogorov–Hinze theory that provides a criterion for the bubble breakup from a force balance has been tested against several results obtained in microgravity experiments. The critical Weber number of this theory was estimated in two different ways: by investigating the behaviour of bubbles of different diameters and by analysing how the mean deformation relates to the mean turbulence intensity. It turns out that, when the turbulence is the single cause of deformation, a minimum Weber number of about 5 is necessary for breakup. Equivalent experiments done by Senhaji (1993) in the presence of a mean drift induced by gravity led to a critical Weber number close to 0.25, about 20 times less than in the present experiments. A similar remark can be made about the study by Sevik & Park (1973). Thus, whenever another cause of breakup superimposes on the turbulent excitation, the Kolmogorov–Hinze theory is insufficient to take into account the additional mechanism of deformation. The critical value of the Weber number is expected to be universal when turbulence is the single cause of deformation: it should be close to 5. However, the theory is still incomplete as was shown in the present study.

Indeed the role of the bubble dynamics in deformation and breakup was identified. On the one hand, the time response of the bubble determines the maximum amount of energy which can be extracted from each eddy. On the other hand, the bubble accumulates energy in its oscillatory deformation. Depending whether the eddy excitation is in phase or not with the bubble oscillations, the deformation increases or decreases. Nevertheless, it has been shown that, on average, the deformation increases continuously. It follows that two breakup mechanisms are possible. The first corresponds to the classical force balance interpretation: intense enough turbulent eddies cause the sudden breakup of a previously non-deformed bubble. The second involves a resonance-like mechanism which requires that the oscillation damping time be larger than the eddy separation.

The role of the bubble dynamics and the occurrence of these two mechanism can be taken into account by the introduction of the mean efficiency coefficient C_d which depends on the bubble diameter and the residence time of the bubble. Its determination involves knowledge of the time succession of velocity fluctuations. Given the lack of general theory on this subject, the turbulence signals have to be obtained from measurements. Then, in the limit of the linear theory, the statistics of deformation can be computed from the turbulence statistics by the use of simulations.

Finally, we wish to stress the importance of the residence time. The experimental determination of a critical number characterizing the breakup is very difficult because the statistics of turbulence maxima converge very slowly. Furthermore it provides little useful information. Here, by introducing the distribution function of the maximum deformation, the influence of the residence time was quantified. The strong dependence of the statistics of deformation on the residence time was thereby demonstrated. It involves two aspects. The first is related to the increase with time of the probability of occurrence of large turbulent fluctuations. The second is due to the accumulation of energy from successive eddies; it can be analysed from the time dependence of the mean efficiency parameter.

The authors would like to thank the Centre National d'Etudes Spatiales and the European Space Agency for their financial and technical support, D. Veynante for his help on spectral analysis, and C. Bongiovanni for the video processing.

REFERENCES

Batchelor, G. K. 1953 *The Theory of Homogeneous Turbulence*. Cambridge University Press.

Bongiovanni, C. 1996 Traitement d'images appliqué à la détermination de la taille, de la vitesse et de la déformation des bulles. Thesis, INP Toulouse.

Bongiovanni, C., Chevaillier, J.-P. & Fabre, J. 1997 Sizing of bubbles by incoherent imaging. *Exps. Fluids* **23**, 209–216.

Calabrese, R. V., Chang, T. P. K. & Dang, P. T. 1986*a* Drop breakup in turbulence stirred-tank contactors. Part 1: Effect of dispersed-phase viscosity. *AIChE J.* **32**, 657–666.

Calabrese, R. V., Wang, C. Y. & Bryner, N. P. 1986*b* Drop breakup in turbulent stirred-tank contactors. Part 3: Correlations for mean size and drop size distribution. *AIChE J.* **32**, 677–681.

Chen, C. H. 1982 *Nonlinear Maximum Entropy Spectral Analysis Methods for Signal Recognition*. Research Studies Press.

Collins, S. B. & Knudsen, J. G. 1970 Drop-size distribution produced by turbulent pipe flow of immiscible liquids. *AIChE J.* **16**, 1072–1080.

Coulaloglou, C. A. & Tavlarides, L. L. 1977 Description of interaction processes in agitated liquid–liquid dispersions. *Chem. Engng Sci.* **32**, 1289–1297.

Delichatsios, M. A. 1975 Model for the breakup rate of spherical drops in isotropic turbulent flows. *Phys. Fluids* **18**, 622–623.

Hesketh, R. P., Etchells, A. W. & Fraser Russell, T. W. 1987 Bubble size in horizontal pipelines. *AIChE J.* **33**, 663.

Hesketh, R. P., Etchells, A. W. & Fraser Russell, T. W. 1991 Experimental observations of bubble breakage in turbulent flow. *Ind. Engng Chem. Res.* **30**, 835–841.

Hinze, J. O. 1955 Fundamentals of the hydrodynamics mechanism of splitting in dispersion processes. *AIChE J.* **1**, 289–295.

Kang, I. S. & Leal, L. g. 1990 Bubble dynamics in time-periodic straining flows. *J. Fluid Mech.* **218**, 41–69 pp. 1380–1418.

Karabelas, A. J. 1978 Droplets size spectra generated in turbulent pipe flow of dilute liquid/liquid dispersions. *AIChE J.* **24**, 170–180.

Kay, S. M. & Marple, S. L. 1981 Spectrum Analysis – a modern perspective. *Proc. IEEE* **69**, November 1981, pp. 1380–1418.

Kolmogorov, A. N. 1949 On the disintegration of drops in a turbulent flow. *Dokl. Akad. Nauk., SSSR*, **66**, 825.

Lamb, H. 1932 *Hydrodynamics*. Cambridge University Press.

Nyström, E. J. 1925 *Acta Soc. Sci. Fennicae*, **50**.

Preumont, A. 1990 *Vibrations Aléatoires et Analyse Spectrale*. Presses Polytechniques Universitaires Romande, Lausanne, Suisse. (Republished in English *Random Vibration and Spectral Analysis*. Kluwer 1994).

Rayleigh Lord 1879 On the capillary phenomena of jets. *Proc. R. Soc. Lond.* **29**, 71–97.

Risso, F. 1994 Déformation et rupture d'une bulle dans une turbulence diffusive. Thesis, INP Toulouse.

Risso, F. & Fabre, J. 1997 Diffusive turbulence in a confined jet experiment. *J. Fluid Mech.* **337**, 233–261.

Senhaji, R. 1993 Qualification globale du fractionnement d'une phase dispersée de faible viscosité en fonction des propriétés turbulentes de l'écoulement externe. Thesis, Ecole Centrale de Nantes.

Sevik, M. & Park, S. H. 1973 The splitting of drops and bubbles by turbulent fluid flow. *Trans. ASME: J. Fluids Engng*, March, 53–60.

Shreekumar, R., Kumar, R. & Gandhi, K. S. 1996 Breakage of a drop of inviscid fluid due to a pressure fluctuation at its surface. *J. Fluid Mech.* **328**, 1–17.

Sleicher, C. A. 1962 Maximum stable drop size in turbulent flow. *AIChE J.* **8**, 471–477.

Stone, H. A. & Leal, L. G. 1989 The influence of initial deformation on drop breakup in subcritical time-dependent flows at low Reynolds numbers. *J. Fluid Mech.* **206**, 223–263.

Swartz, J. E. & Kessler, D. P. 1970 Single drop breakup in developing turbulent pipe flow. *AIChE J.* **16**, 254–260.

Taylor, G. I. 1932 The viscosity of a fluid containing small drops of another fluid. *Proc. R. Soc. Lond.* A **138**, 41–48.

Taylor, G. I. 1934 The formation of emulsions in definable fields of flow. *Proc. R. Soc. Lond.* A **146**, 501–523.

Trinh, E., Zwern, A. & Wang, T. G. 1982 An experimental study of small-amplitude drop oscillations in immiscible liquid systems. *J. Fluid Mech.* **115**, 453–474.

Veynante, D. & Candel, S. M. 1988 Application of nonlinear spectral analysis and reconstruction to laser Doppler velocimetry. *Exps Fluids* **6**, 534–540.

Walter, J. F. & Blanch, H. W. 1986 Bubble breakup in gas–liquid bioreactors: breakup in turbulent flows. *Chem. Engng J.* **32**, B7–B17.

Wang, C. Y. & Calabrese, R. V. 1986 Drop breakup in turbulent stirred-tank contactors. Part 2: Relative influence of viscosity and interfacial tension. *AIChE J.* **32**, 667–676.

Zeitling, M. A. & Tavlarides, L. L. 1972 Fluid–fluid interactions and hydrodynamics. *Can. J. Chem. Engng* **50**, 207–215.